An Algebraic Domain Reprojection, Deep Learning and DNS-data-driven Approach for Turbulence Modeling

Christian J. Lagares-Nieves[1,2*], Subhajit Roy[2†], and Guillermo Araya[2‡]
[1]*Dept. of Mechanical Eng., University of Puerto Rico at Mayaguez, PR 00681, USA.*
[2]*Computational Turbulence and Visualization Lab., Dept. of Mechanical Eng., University of Texas at San Antonio, TX 78249, USA.*

Advanced turbulence modeling remains a cornerstone in optimizing engineering applications, particularly in aerospace, where accurate predictions of turbulent behaviors in high-speed flows are critical. Traditional models often fall short in complex scenarios involving high Mach numbers and strong pressure gradients due to their inherent limitations in handling non-linear dynamics and compressibility effects, not to mention high Reynolds number flows. This manuscript introduces a novel approach that synergistically contrasts algebraic domain reprojection and deep learning techniques to compare the adaptability and accuracy of turbulence models. The proposed Algebraic Semi-Log Compressible Domain Re-Projection Model (ASC-DRM) leverages deep learning to fine-tune model parameters and accurately predict turbulent Reynolds stresses under varying flow conditions. Comprehensive validations of second order statistics against Direct Numerical Simulation (DNS) data demonstrate the model's improved prediction capabilities across a range of Reynolds and Mach numbers. The integration of machine learning not only refines the turbulence model predictions but also paves the way for incorporating more complex physical phenomena into the modeling process, such as thermal effects and chemical reactions. This research marks a significant advancement in the field of computational fluid dynamics by providing a robust framework that significantly enhances the predictive accuracy of turbulence models in compressible flows, thus offering broad implications for design and optimization in aerospace and other engineering fields.

I. Nomenclature

HR	=	High Reynolds number case
LR	=	Low Reynolds number case
R_{δ_2}	=	compressible momentum thickness Reynolds number
M_∞	=	Freestream Mach number
U_∞	=	Freestream velocity
U^+_{VD}	=	Van Driest transform velocity in wall units
T_∞	=	Freestream temperature
T_r	=	Recovery temperature
T_w	=	Wall temperature
u_τ	=	Friction velocity
P	=	Mean pressure
T	=	Mean temperature
k	=	Thermal conductivity
c_p	=	Specific heat at constant pressure
N_x	=	Number of nodes along the streamwise direction
N_y	=	Number of nodes along the wall normal direction

*PhD Research Assistant & Doctoral Candidate, Department of Mechanical Engineering, 259 Alfonso Valdez Blvd., Mayaguez, PR, 00680, and Student Member, christian.lagares@upr.edu

†Postdoctoral Research Associate, Department of Mechanical Engineering, University of Texas at San Antonio, San Antonio, TX, 78249. AIAA Associate Fellow, subhajit.roy@utsa.edu

‡Associate Professor, Department of Mechanical Engineering, University of Texas at San Antonio, San Antonio, TX, 78249. AIAA Associate Fellow, araya@mailaps.org, https://ceid.utsa.edu/garaya/

N_z	=	Number of nodes along the spanwise direction
δ	=	Boundary layer thickness
μ	=	Dynamic molecular viscosity
ν_w	=	Wall kinematic viscosity
ρ	=	Fluid Density
σ	=	Stress tensor
τ	=	Shear stress
Subscript	=	
inl	=	inlet
rec	=	recycle
$_{rms}$	=	Root-Mean Squared
$'$	=	Superscript denotes fluctuating components
∞	=	Subscript denotes freestream quantities

II. Introduction

Turbulence modeling remains a pivotal area of study in computational fluid dynamics (CFD), especially in aerospace engineering where the simulation of fluid flows needs to account for a wide range of speeds from subsonic to supersonic flow regimes. Such models are critical for accurately predicting boundary layer behavior, shock-turbulent boundary layer interactions, and aerodynamic heating-factors that are essential for the design and optimization of aerospace vehicles [1, 2]. The inherent complexities of compressible flows, characterized by substantial variations in fluid properties and dynamic interactions between shock waves and boundary layers, pose significant challenges for conventional turbulence modeling techniques [3]. Among the prevalent methodologies for turbulence modeling, zero-equation models, such as the Baldwin-Lomax model, utilize algebraic relations to estimate turbulent viscosity based on local mean flow properties [4]. Praised for their simplicity and minimal computational demand, these models are particularly advantageous in preliminary design phases where quick and resource-light calculations are necessary [1, 4]. However, their oversimplified nature often limits their effectiveness in capturing more complex flow phenomena such as flow separation, the influence of shock waves, and the effects of curvature and rotation [2, 5, 6].

In contrast, Reynolds-Averaged Navier-Stokes (RANS) methods in conjunction with eddy viscosity models provide a more comprehensive approach by solving additional transport equations to determine Reynolds stresses. Prominent RANS models, like the $k-\omega$ SST and the Spalart-Allmaras model, are renowned for their robustness in managing adverse pressure gradients (APG) and separating flows, commonly encountered in transonic and supersonic regimes [6, 7]. However, the increased fidelity of RANS models comes at the expense of higher computational costs and the need for careful calibration of model constants to align with specific flow conditions [2, 7]. This study endeavors to bridge the gap between the straightforward, computationally efficient zero-equation models and the detailed, high-fidelity RANS approaches. By concentrating on the subsonic to supersonic range, this paper evaluates the capacity of these models to predict turbulent behaviors in compressible flows accurately, specifically excluding extremely high-speed phenomena such as thermal non-equilibrium and ionization, which dominate hypersonic flows [3]. Moreover, review paper by [8] explores the integration of machine learning techniques to refine turbulence model predictions, offering a novel approach to enhance the predictive accuracy of these models by leveraging existing comprehensive datasets.

Recent advancements in machine learning (ML), particularly deep learning, have shown promising potential in revolutionizing CFD and other physics-based simulations. These techniques offer novel approaches to longstanding challenges in these fields, such as turbulence modeling, flow prediction, and multi-scale dynamics where traditional numerical methods face strong encumbrances. One of the foundational studies by Ling et al. (2016) [9] introduced deep neural networks to predict discrepancies in Reynolds-Averaged Navier-Stokes (RANS) simulations, addressing traditional turbulence modeling's deficiencies. Similarly, Thuerey et al. (2020) [10] demonstrated that convolutional neural networks could effectively predict complex flow fields around arbitrary objects, reducing computational costs significantly. Moreover, the work by Xu et al. (2020) [11] on using generative adversarial networks (GANs) highlighted how ML could enhance data efficiency, a crucial advancement for resource-intensive simulations in CFD. Furthermore, the concept of Physics-Informed Neural Networks (PINNs) introduced by Raissi et al. (2019) [12] integrates physical laws directly into the learning process, ensuring adherence to known principles and enhancing model reliability. This approach has been extended by recent contributions such as those by Yousif et al. (2023) [13], who developed a deep-learning approach for reconstructing 3D turbulent flows from 2D observations, pushing the boundaries of data-derived insights in fluid mechanics. In addition, recent emerging studies like those by Buaria and Sreenivasan

(2023) [14] explore the capabilities of deep neural networks in forecasting small-scale dynamics of fluid turbulence, offering deeper insights into the chaotic nature of turbulence. These studies are complemented by research into embedded training of neural-network subgrid-scale models, as demonstrated by MacArt et al. (2021) [15], which further bridges the gap between theoretical fluid dynamics and practical, scalable ML applications. Each of these studies underscores the transformative potential of machine learning in fluid dynamics, setting the stage for more accurate, efficient, and flexible simulations across various scientific and engineering disciplines. As these methodologies evolve, they promise to reshape our understanding and capabilities within the realm of CFD and beyond. However, considerations from generalization potential, computational cost and robustness ought to be present in every analysis made on deep learning methodologies. The attractive nature of these methods should not cloud the potential to advance other avenues even if by drawing inspiration from DL-based approaches. This feedback loop of information distillation can be critical to the evolution of turbulence modeling and other crucial fields in computational physics.

Furthermore, this study extends into the application of advanced data-driven methods to overcome traditional limitations of empirical and semi-empirical turbulence models. These methods, including deep learning and reinforcement learning, are employed to dynamically adjust model coefficients or to propose new model forms based on direct simulation data, promising substantial improvements in accuracy and reliability over classical models. This paper is structured as follows: Section III outlines the numerical setup, including solver configurations and grid independence studies. Sections IV and V present a detailed discussion on the results obtained from the computational models, emphasizing their performance across different flow regimes. Section VI summarizes the findings and suggests future directions for advancing turbulence modeling techniques within aerospace applications.

III. Governing Equations and Inflow/Boundary Conditions

In this study, we examine the dynamics of compressible subsonic/supersonic spatially-developing turbulent boundary layers (SDTBL) through direct numerical simulations (DNS), applying the compressible Navier-Stokes equations under the assumption of low Knudsen numbers and disregarding non-equilibrium effects [16]. We have also included in this scrutiny, DNS of incompressible SDTBL for compressibility effect analysis and challenge assessment for turbulence modeling. For clarity and reader's convenience, we present the fundamental conservation equations for mass, momentum, and energy (strong formulation) in Equations 1, 2, and 3, respectively.

$$\frac{\partial \rho}{\partial t} + \frac{\partial}{\partial x_j}\left(\rho u_j\right) = 0 \tag{1}$$

$$\frac{\partial \rho u_i}{\partial t} + \frac{\partial}{\partial x_j}\left(\rho u_i u_j + p\delta_{ij} - \sigma_{ij}\right) = 0 \tag{2}$$

$$\frac{\partial \rho e}{\partial t} + \frac{\partial}{\partial x_j}\left((\rho e)u_j - u_i\sigma_{ij} + q_j\right) = 0 \tag{3}$$

where ρ is the density; u_i is the velocity component in the i-direction; p is the pressure; σ_{ij} is the stress tensor modeled as a linear stress-strain relationship,

$$\sigma_{ij} = 2\mu S_{ij} - \frac{2}{3}\mu\delta_{ij}S_{kk} \tag{4}$$

and S_{ij} is the strain rate tensor defined as $\frac{1}{2}\left(\frac{\partial u_i}{\partial x_j} + \frac{\partial u_j}{\partial x_i}\right)$; μ represents the dynamic fluid viscosity; and q_i is the heat flux modeled via the Fourier's law as $q_i = -\kappa\frac{\partial T}{\partial x_i}$, where κ is the thermal fluid conductivity; e is total energy per unit mass, assumed to be:

$$e = c_v T + \frac{1}{2}u_i^2 \tag{5}$$

with c_v as the specific heat at constant volume. Furthermore, the dynamic fluid viscosity is modeled to vary according to the following power law function:

$$\mu = \mu_\infty \left(\frac{T}{T_\infty}\right)^{0.76} \tag{6}$$

The 0.76-power law variation of the dynamic fluid viscosity mirrors the well-established Sutherland's viscosity law in its predictive accuracy for DNS simulations, where equation 6 is more suitable for non-dimensional governing equations.

In all cases, a molecular Prandtl number of 0.72 is assumed. Furthermore, for a perfect gas the equation of state is employed, i.e. $p = \rho RT$ where R is the gas constant.
The governing equations of the flow are presented in their strong form; however, we apply the weak formulation in our finite element flow solver. The DNS utilizes the PHASTA (Parallel Hierarchic Adaptive Stabilized Transient Analysis) flow solver [17], which is based on a Finite Element approach (FEM) with a SUPG (Streamline Upwind Petrov-Galerkin) stabilization of the convectives terms [18, 19]. In order to obtain the Galerkin weak formulation, the strong form is multiplied by an arbitrary vector w, performing the integration over the whole domain for interior and boundary elements and including the stabilization integral or SUPG. In short, the integrals are solved using Gauss quadrature, obtaining a system of non-linear ordinary differential equation system. Later, the generalized-α time method is employed to generate a non-linear system of algebraic equations. Finally, the system is linearized by the Newton method and is solved at each Newton iteration. The numerical scheme is 2^{nd} order accurate in space with fully implicit time integration (2^{nd} order accurate). Readers interested in the finite element approach are referred to [20, 21]. PHASTA has been extensively validated in numerical flow simulations with high spatial/temporal resolution [22–27]

Key considerations for effective DNS of SDTBL include: (i) a sufficiently expansive computational domain to encompass the largest scale motions (LSM); (ii) the mesh resolution must be adequate in order to capture the smallest turbulence momentum/thermal scales (Kolmogorov and Batchelor scales), (iii) the introduction of accurate, unsteady inflow turbulent fluctuations; and (iv) ensuring the turbulent inflow exhibits a natural power spectrum to reduce the length of the "inlet developing section" (ideally 2-3 δ_{inl}'s). The Dynamic Multiscale Approach (DMA) for inflow generation, as proposed by Araya *et al.* [28] and adapted to compressible SDTBL [22–26], uses a modified version of the rescaling-recycling technique by Lund *et al.* [29]. Our choice of inflow condition generation for compressible turbulent layers has proven to be highly effective, achieving minimal development regions (at most $2.5\delta_{inlet}$) and an energy spectrum akin to fully turbulent flow [25]. The key aspect of the rescaling-recycling method is the extraction, and scaling law application (mapping) over the flow solution ("on the fly" time-averaged and fluctuating components of velocity, thermal, and pressure fields) from a downstream plane, to finally reintroduce the transformed instantaneous profiles (time-averaged plus fluctuations) at the inlet of the computational domain. Our lessons learned confirm that maintaining constant mean pressure at the inlet provides more stable and precise simulations than when re-injecting pressure fluctuations (notice that, still, fluctuations of the density exist at the inlet plane according to the equation of state and the fluctuating thermal field. This is consistent with works by [30] and [31], where they stated that pressure fluctuations at the inlet are minimal relative to temperature fluctuations. The Reynolds decomposition applied to the instantaneous parameters separates them into a time-averaged and a fluctuating component, ensuring detailed representation of flow characteristics.

A. Favre-Averaged Equations

To extend the discussion on the dynamics of compressible supersonic turbulent boundary layers (SDTBL) by incorporating Favre averaging into the governing equations, let's begin with the foundation laid out by the direct numerical simulations (DNS) and the Navier-Stokes equations. Favre averaging [32], is particularly suitable for turbulent compressible flows as it provides a mass-weighted averaging method that preserves the conservation form of the equations. This approach is essential when dealing with the variable density characteristic of compressible flows. We'll apply Favre averaging to the fundamental conservation equations for mass, momentum, and energy presented earlier, transforming them into their Reynolds-averaged Navier-Stokes (RANS) counterparts suitable for analysis of turbulent flows.
The Favre average of a quantity ϕ is defined as $\tilde{\phi} = \frac{\overline{\rho\phi}}{\overline{\rho}}$, where the overbar denotes a Reynolds average. Applying this to the velocity components u_i and other flow variables, we can derive the Favre-averaged forms of the governing equations. The mass conservation equation (Equation 1) remains unchanged under Favre averaging because it is linear in terms of ρ and u_i:

$$\frac{\partial \overline{\rho}}{\partial t} + \frac{\partial}{\partial x_j}\left(\overline{\rho}\tilde{u}_j\right) = 0 \tag{7}$$

For momentum conservation (Equation 2), applying Favre averaging yields:

$$\frac{\partial \overline{\rho}\tilde{u}_i}{\partial t} + \frac{\partial}{\partial x_j}\left(\overline{\rho}\tilde{u}_i\tilde{u}_j + \overline{p}\delta_{ij} - \overline{\sigma}_{ij}\right) = -\frac{\partial}{\partial x_j}(\overline{\rho u_i'' u_j''}) \tag{8}$$

where $u_i'' = u_i - \tilde{u}_i$ represents the Favre fluctuation component of the velocity. The term $\overline{\rho u_i'' u_j''}$ signifies the Reynolds

stress tensor resulting from turbulence.
Energy conservation (Equation 3) becomes:

$$\frac{\partial \overline{\rho}\tilde{e}}{\partial t} + \frac{\partial}{\partial x_j}\left((\overline{\rho}\tilde{e})\tilde{u}_j - \tilde{u}_i\overline{\sigma}_{ij} + \overline{q}_j\right) = -\frac{\partial}{\partial x_j}(\overline{\rho e'' u_j''}) \tag{9}$$

where $\tilde{e} = c_v\tilde{T} + \frac{1}{2}\tilde{u}_i\tilde{u}_i$ represents the Favre-averaged total energy per unit mass, and $e''u_j''$ denotes the turbulent flux of energy.
The expressions for the stress tensor σ_{ij} and heat flux q_i remain unchanged in their forms but are evaluated using the Favre-averaged variables and include additional terms to account for the turbulent fluctuations:

$$\overline{\sigma}_{ij} = 2\overline{\mu}\tilde{S}_{ij} - \frac{2}{3}\overline{\mu}\delta_{ij}\tilde{S}_{kk} \tag{10}$$

$$\overline{q}_i = \overline{\kappa}\frac{\partial \tilde{T}}{\partial x_i} \tag{11}$$

The Favre-averaged strain rate tensor is $\tilde{S}_{ij} = \frac{1}{2}\left(\frac{\partial \tilde{u}_i}{\partial x_j} + \frac{\partial \tilde{u}_j}{\partial x_i}\right)$. The dynamic viscosity μ and thermal conductivity κ follow the power law and Fourier's law, respectively, based on Favre-averaged temperature $\tilde{T}$.
In this work, we aim to assess the ability of two models to "close" the Favre-averaged Navier stokes equations. Specifically, we aim to model $\overline{\rho u_i'' u_j''}$ and explicitly disregard the closure problem in the similarly complex energy equation ($\overline{\rho e'' u_j''}$) which will be considered in a future work.

B. Postprocessing Toolkit

To address the challenges of processing extensive computational domains and extracting insights from large-scale simulations, we have developed an in-house, scalable, out-of-core post-processing framework named Aquila, which is Latin for "eagle." This name symbolizes our goal of enabling domain experts to ascend beyond the complexities of low-level computational details, much like an eagle soaring above storms, while still achieving outstanding performance and scalability across various computing environments—from laptops to workstations, and from small clusters to large-scale facilities with both CPU and GPU capabilities. Aquila, currently transitioning from its second to third major iteration, is illustrated in Figure 1.

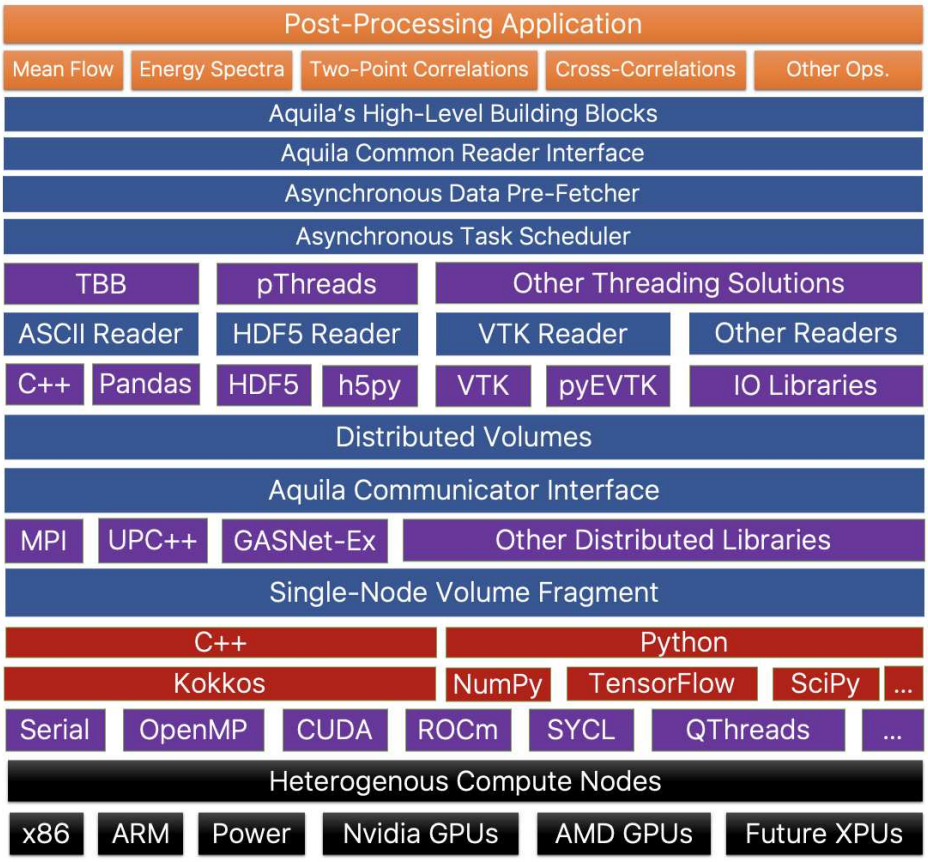

Fig. 1 Overview of the software architecture for Aquila.

Presently, Aquila leverages TensorFlow [33] as its computational backend, enabling efficient execution on CPUs and GPUs from multiple hardware vendors. Domain decomposition is managed via MPI [34], optimizing performance in large-scale computing settings. Aquila demonstrates robust strong scaling capabilities on both CPUs and GPUs, as shown in Figure 2. Users can seamlessly switch between CPU and GPU targets without modifying their scripts, thanks to the backend flexibility provided by TensorFlow. Aquila's efficiency is evidenced by its ability to compute mean flow and a suite of "Quantities of Interest" (QoI), which include fluid velocity, pressure, thermal fluctuations, boundary layer characteristics, turbulent kinetic energy, various correlations, and over a million spanwise energy spectra. The analysis is based on a dataset comprising roughly 4000 flow fields, totaling about 8.3 TB—too voluminous for traditional in-memory processing on standard systems. Instead, Aquila cleverly manages this data on non-volatile storage media, creating the effect of an in-memory operation through strategic asynchronous data prefetching. Overall, Aquila's parallel scaling efficiency exceeds 80%, with GPU implementations typically outperforming CPU setups by a factor of two. This is particularly apparent in tasks with high computational demands, as depicted in Figure 2, where GPUs excel in throughput-oriented tasks. The integration of an asynchronous prefetcher alone enhances total runtime by approximately 23-24%, culminating in a combined speedup of roughly 2.48 times compared to a CPU-only configuration without prefetching.

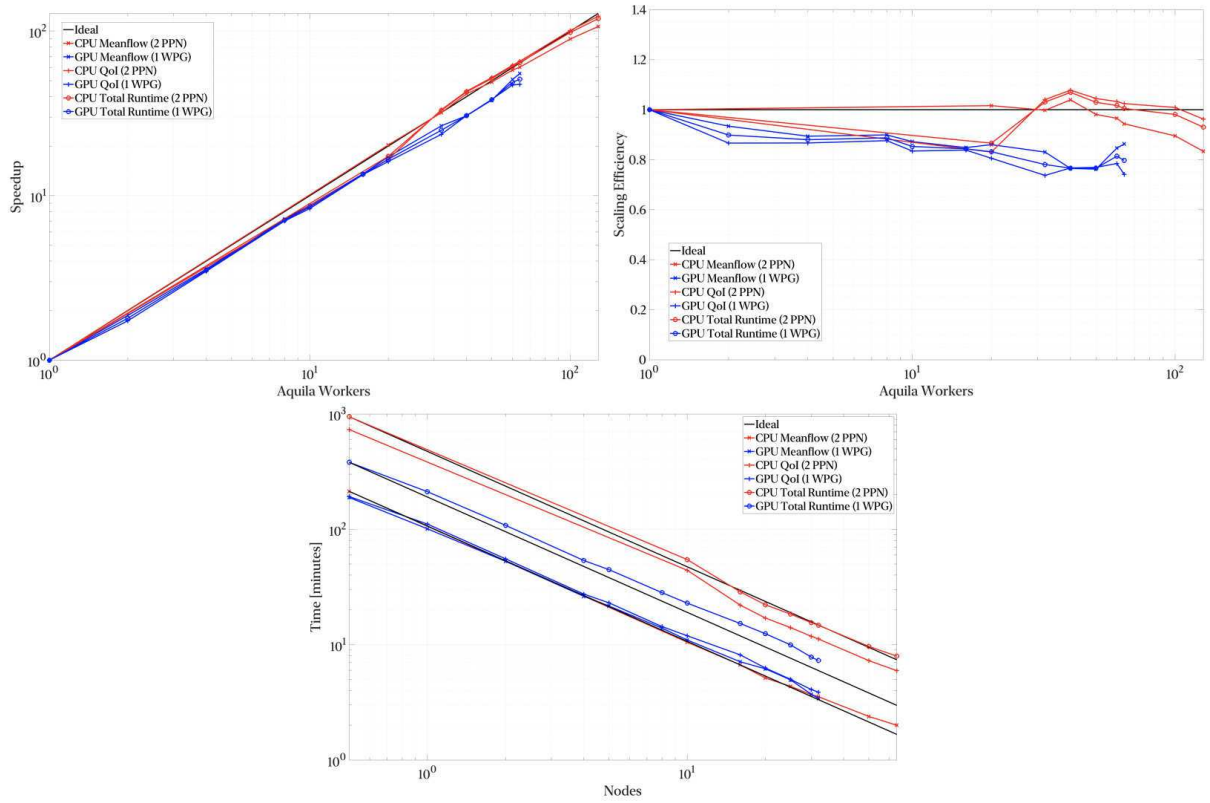

Fig. 2 Depiction of Aquila's strong scaling across different configurations: CPU-only nodes with two processes each (top-left), threading across additional CPU cores (top-right), and GPU nodes utilizing two GPUs per node with one MPI rank per GPU (bottom).

C. DNS Cases at Low and High Reynolds Numbers

Table 1 depicts information regarding the principal parameters of DNS databases employed in this study at high Reynolds numbers, such as the freestream Mach number (IC stands for incompressible), the incompressible ($Re_\theta = \rho_\infty U_\infty \theta/\mu$) or compressible momentum thickness Reynolds number ($Re_{\delta 2} = \rho_\infty U_\infty \delta_2/\mu_w$), domain dimensions as a function of the inlet 99% boundary layer thickness (δ_{inl}), and mesh resolution details are supplied. It is worth highlighting that mesh resolution in wall units is defined based on inlet friction velocity (the largest values in the domain). In all compressible cases, wall adiabatic conditions were assumed. Figure 3 (a) shows a computational domain schematic, whereas fig. 3 (b) exhibits images of the DNS mesh. For the four cases considered in present study, the number of grid points is the same: 990×250×210, indicating the grid points along the streamwise (x), wall-normal (y) and spanwise (z) direction, respectively, totalling around 52-million points. The cases were run in 1200 CPU cores at the Onyx supercomputer (ERDC DSRC, DoD HPC) and Narwhal supercomputer (Navy DSRC, DoD HPC), consuming approximately 900K CPU core hours each.

Similarly

Figure 4 shows first and second order statistics for the incompressible and subsonic flat plate. The Van Driest transformation was considered for the mean streamwise velocity (U^+_{VD}) at M_∞ = 0.8. External DNS data from [35] at similar Reynolds numbers is also included. As seen in fig. 4 (a), the agreement of present DNS results, including the subsonic case (the Van Driest transformation compensates quite well density variation), is encouraging excepting in the wake region that can be attributed to some Reynolds number dependency. Lengthy log regions are observed (about 200 wall units) in all cases due to the high Reynolds numbers resolved. Turbulence intensities and Reynolds shear stresses (2^{nd} order statistics) are plotted in figure 4 (b). It can be stated that compressibility effect is almost negligible at M_∞ = 0.8. Turning to higher order statistics, fig. 5 depicts skewness and flatness of streamwise velocity fluctuations, u'. Positive values of S_u in the near wall region ($y^+ < 10$) indicate that u' distribution are positive skew, while the contrary occurs towards the edge of the boundary layer, as seen in fig. 5 (a). We have detected a moderate compressibility

effect on S_u close to the wall. Flatness or 4^{nd} order statistics profiles are exhibited by fig. 5 (b), which represents the peakedness of a distribution, in this case of u'. Furthermore, the flatness or kurtosis is and indicator of the presence of high-amplitude events. For a Gaussian distribution, the flatness is 3. Thus, larger values of flatness in turbulence means the occurrence of intense, sporadic events (intermittency), leading to a distribution with heavier tails compared to the Gaussian distribution. The flatness values higher than 3 in the linear viscous sublayer ($y^+ < 5$) demonstrate a non-Gaussian distribution of u'. The distribution of u' in the log region follows a quasi-Gaussian or normal distribution given the values of F_u around 3 (also, $S_u \approx 0$ in that region). Figure 6 shows a comparison of present DNS results at $M_\infty = 1.6$ with DNS data from [36] at a slightly higher Mach number ($M_\infty = 2$) for first and second order statistics. The agreement in all cases is very good, major discrepancies were observed in peaks of u'^+_{rms} distribution ($\sim 5\%$). In terms of the skewness and flatness distribution for supersonic cases, present Mach-1.6 DNS results almost overlap with DNS by [36] at $M_\infty = 2$. Readers are referred to our previous work for additional DNS validation of incompressible and high supersonic cases [22, 25], as well as for the DNS databases at low Reynolds numbers in Table 2 ([24, 37]).

Table 1 Information of DNS databases at high Reynolds numbers.

Case	Type	Mach	Re_θ or $Re_{\delta 2}$	$L_x \times L_y \times L_z$	$\Delta x^+, \Delta y^+_{min}, \Delta y^+_{max}, \Delta z^+$
1HR	Incompressible	IC	2000-2400	$16\delta_{inl} \times 3\delta_{inl} \times 3\delta_{inl}$	11.5, 0.2/10, 10
2HR	Subsonic	0.8	2066 – 2468	$15.1\delta_{inl} \times 3\delta_{inl} \times 3\delta_{inl}$	11.9, 0.2/11, 11
3HR	Low Supersonic	1.6	2370 – 2846	$14.9\delta_{inl} \times 3\delta_{inl} \times 3\delta_{inl}$	12.7, 0.2/11, 12
4HR	High Supersonic	2.86	3171 – 3743	$15.1\delta_{inl} \times 3\delta_{inl} \times 3\delta_{inl}$	12.5, 0.2/11, 11.8

Table 2 Information of DNS databases at low Reynolds numbers.

Case	Type	Mach	Re_θ or $Re_{\delta 2}$	$L_x \times L_y \times L_z$	$\Delta x^+, \Delta y^+_{min}, \Delta y^+_{max}, \Delta z^+$
1LR	Incompressible	IC	306 – 578	$45\delta_{inl} \times 3.5\delta_{inl} \times 4.3\delta_{inl}$	14.7, 0.2/13, 8
2LR	Subsonic	0.8	309 – 570	$42.8\delta_{inl} \times 3.3\delta_{inl} \times 4\delta_{inl}$	14, 0.18/13.4, 7.8
3LR	Low Supersonic	1.6	350 – 629	$43.2\delta_{inl} \times 3.3\delta_{inl} \times 4.1\delta_{inl}$	14.2, 0.19/14.4, 7.86
4LR	High Supersonic	2.86	468 – 831	$43.4\delta_{inl} \times 3.4\delta_{inl} \times 4.15\delta_{inl}$	15.5, 0.2/16, 8.6

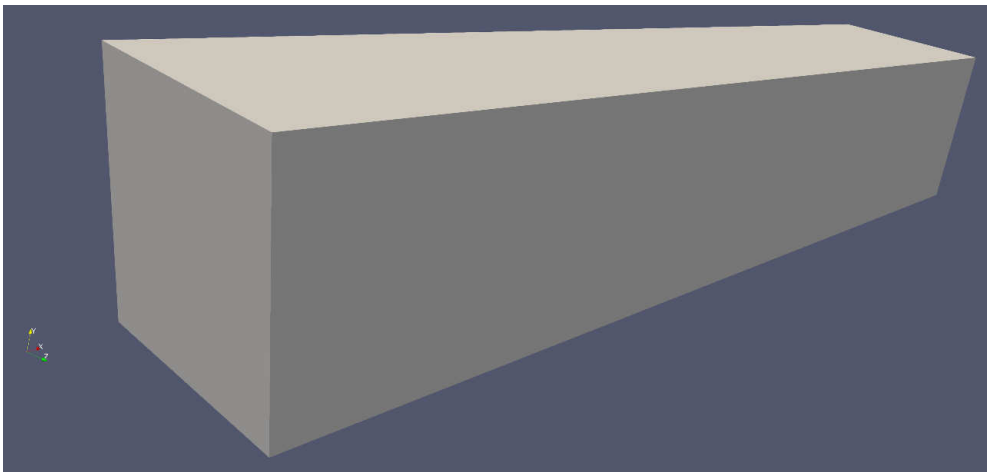

(a)

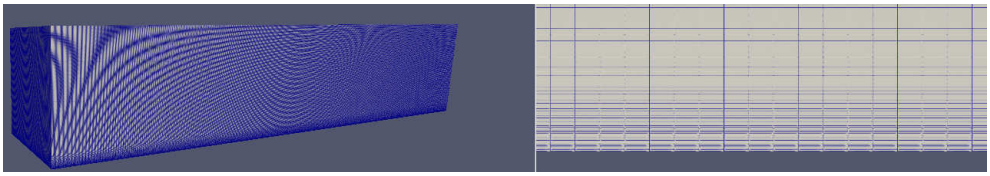

(b)

Fig. 3 (a) Schematic of computational box, (b) DNS mesh (left) and mesh close-up in near wall region (right).

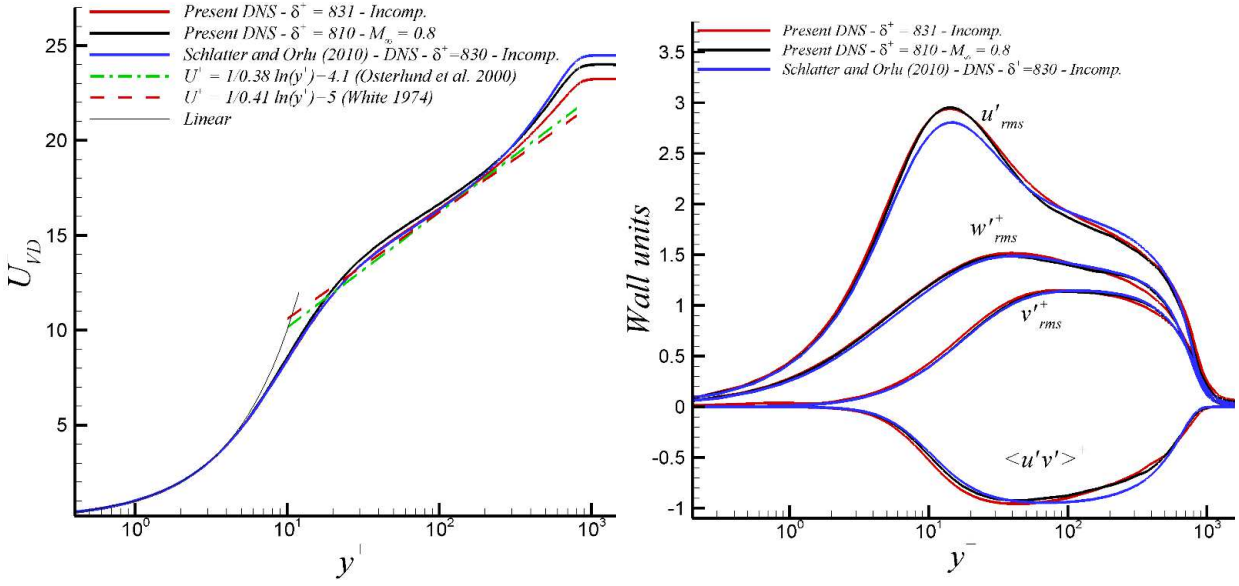

(a) (b)

Fig. 4 (a) Van Driest transformation of the mean streamwise velocity, (b) turbulence intensities and Reynolds shear stresses for incompressible and subsonic cases, all in wall units.

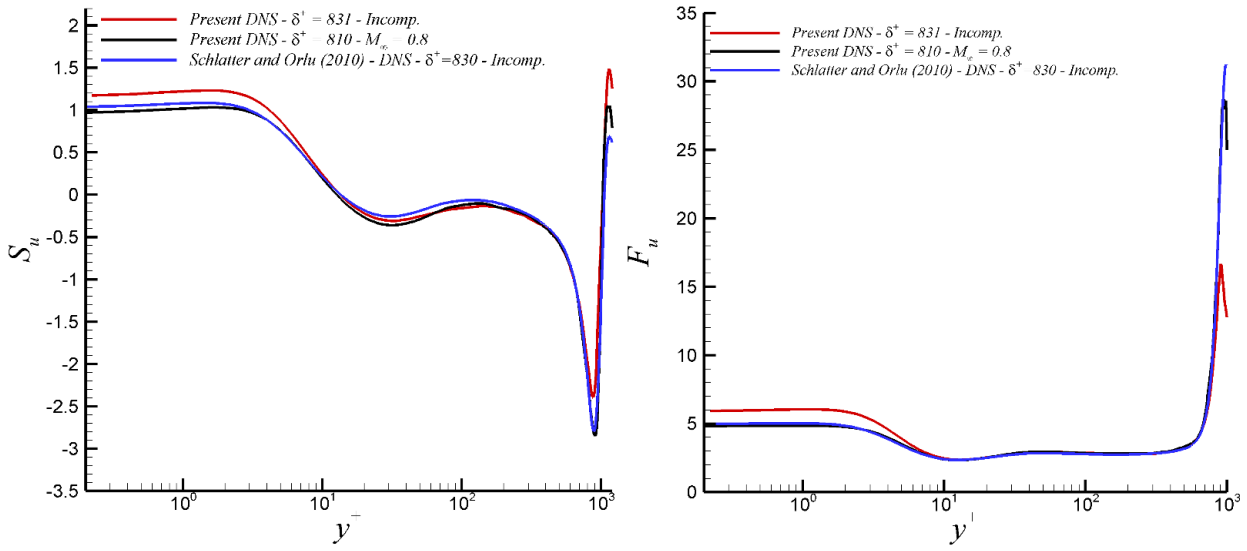

(a) (b)

Fig. 5 (a) Skewness, (b) flatness of streamwise velocity fluctuations for incompressible and subsonic cases, all in wall units.

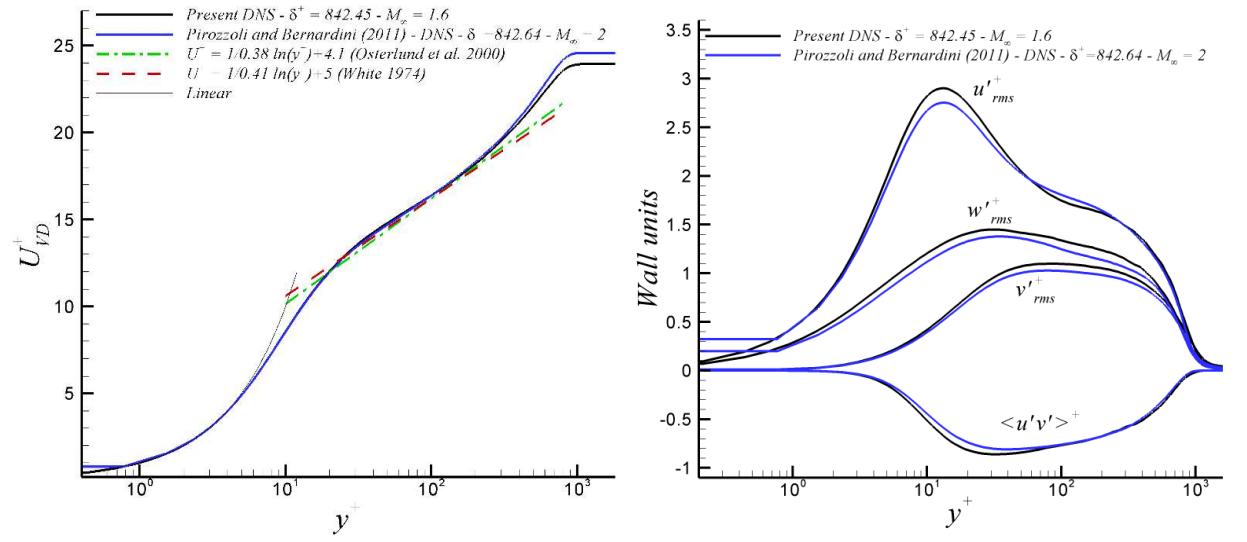

(a) (b)

Fig. 6 (a) Van Driest transformation of the for mean streamwise velocity, (b) Turbulence intensities and Reynolds shear stresses for low supersonic cases, all in wall units.

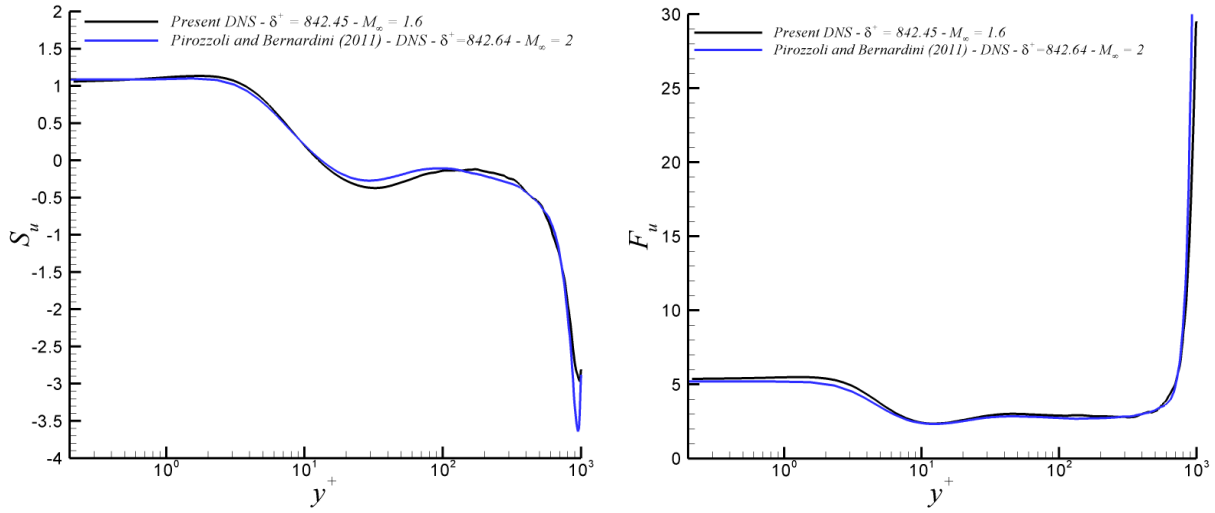

(a) (b)

Fig. 7 (a) Skewness, (b) flatness of streamwise velocity fluctuations for low supersonic cases, all in wall units.

IV. Inverse Formulation of the Reynolds Stresses

A. Data-Driven Turbulence Modeling

1. Neural Network Architecture

The final design of the neural network took many iterations to refine and is still likely far from optimal in many regards. However, in this section we will explore the rationale for its design. The neural network is a feed-forward neural network with 12 layers in a base network followed by additional, 12-layer networks per non-zero entry in the stress tensor. The layers are grouped into 3 layer modules with residual connections and a modified softplus function. The overall schematic can be seen in figure 8. The modified softplus incorporates an additional fixed term and can be expressed as (along its first and second derivatives):

$$f(x) = \log(1 + e^x) - \log(2) \tag{12}$$

$$f'(x) = \frac{e^x}{(e^x + 1)} \tag{13}$$

$$f''(x) = \frac{e^x}{(e^x + 1)^2} \tag{14}$$

This activation function was chosen because the optimization procedure involved a loss function with first derivatives of the output terms w.r.t. some of the inputs. Calculating gradients of these requires calculating second derivatives. Initially, we explored other possible activation functions such as the ReLU and ELU, but these have either a null or discontinous second derivative. The softplus function is infinitely differentiable (i.e., it is a C^∞ function). This allows for a second order constraint based on equation 8.

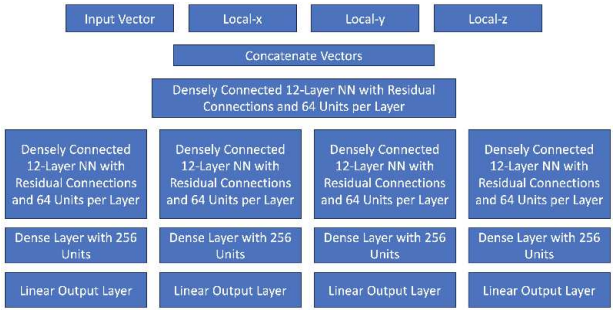

Fig. 8 NN Architecture Schematic

We also include a linear modification as part of each output path since typical output values tend to be small. This enables the network to operate on larger values internally that are then scaled down to the actual operating range. This was done after observing difficulties in earlier versions of the models since all of the values were fairly small and hard to accurately discriminate since errors were "small" in magnitude. This also informed one additional linear transformation based on knowledge of the underlying physics of the problem. For the $\overline{\rho u'' v''}$ output path, we also invert the sign of the output by multiplying the same output scaling function by -1. This change, while subtle allows all of the outputs to be positive internally and yielded large improvements to overall model quality as will be showcased later in the manuscript.

Our neural network models were trained using Stochastic Gradient Descent (SGD) with momentum, a method chosen for its efficacy in handling complex datasets, as outlined in [38]. We set the momentum to 0.9 and started with a learning rate of 0.1, linearly decaying it to 0.0001 over 100 epochs. This approach allowed for precise weight adjustments, enhancing model convergence. Empirically, a batch size of 2048 proved optimal, significantly outperforming smaller sizes like 32 in terms of error rates and training efficiency. The training, conducted on a Tesla V100 GPU for about 60 hours (equivalent to 50 epochs over 14.62 million training samples), demonstrated the model's robustness. The validation and test dataset contained 4.87 million samples, further validating the model's performance and our optimization strategy.

B. Evaluation and Short-Comings of an Inverse Formulation

In this section, we will explore the individual impact of each entry in the Reynolds's stress tensor throughout a boundary layer for the High Re cases in table 1. This is often as important (if not more) than global error metrics because it sheds light on the physics of the boundary layer. As previously outlined, we will focus on four terms, three normal and one shear stress. All of the results are "inner-scaled" which normalizes the results using viscous units using parameters "at the wall." The first of the normal stresses, $\rho u''u''$, can be seen in figure 9. For all Mach numbers, DNS and NN results show good agreement, especially in the near-wall region ($y^+ < 50$). However, there are discrepancies further away from the wall, especially for higher Mach numbers. The magnitude of the peak increases with Mach number, indicating that compressibility effects enhance turbulent fluctuations. In general, the location of the main peak is accurately captured by the DNN. The slight amount of over/undershooting is common to RANS models and it is actually reasonable for such an early attempt at a generalized explicit model.

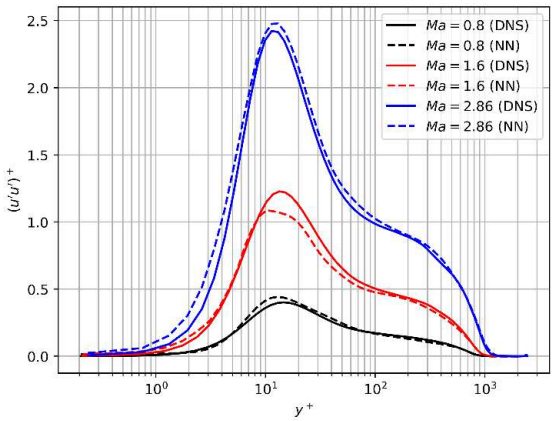

Fig. 9 Comparison of the $\rho u''u''$ term for DNS and NN output

Earlier, we mentioned an optimization related to the output of $\rho u''v''$ whose average in time is typically negative for many typical flows and reference coordinate systems. This Reynolds shear stress is a primary contributor to momentum transfer in a turbulent flow. Given the typical negative values and the activation functions throughout the network (which are biased towards positive outputs), this term had the "toughest" time in an earlier iteration of the network architecture where no sign information was encoded into the NN design. This can be seen in figure 10a which exhibited wild oscillations and violent over/undershooting. Allowing the network to internally operate on positive values and "inverting" the values as part of the aforementioned scaling operation, greatly improved the overall model quality (for all tensor values) with a particularly notable improvement in the Reynolds shear stress $\rho u''v''$ as can be clearly seen in figure 10b. The peak negative values near the wall indicate the highest shear and hence the strongest momentum exchange. The NN seems to slightly overpredict the shear stress magnitude for the highest Mach number at certain y^+ positions, indicating potential discrepancies in the NN's ability to capture the effects of compressibility on turbulent mixing. Also, this term tends to be the most challenging to model numerically. There is still a large margin for improvement, but in general, the quality of the prediction is acceptable.

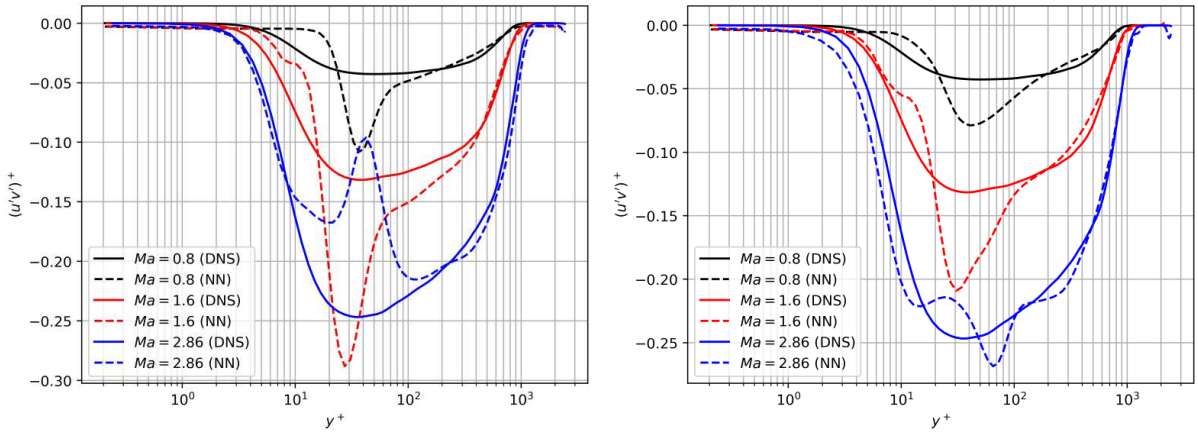

(a) (b)

Fig. 10 Comparison of the $\rho u''v''$ term for DNS and NN output for (a) an earlier model iteration and (b) the most recent iteration considering sign inversion as part of the model formulation

The wall-normal ($\rho v'v'$) and spanwise normal ($\rho w'w'$) Reynolds stresses, seen in figures 11 and 12, are crucial components in the characterization of turbulence, particularly in the context of boundary layer dynamics and turbulence modeling. These stresses not only indicate the energy distribution within a turbulent flow but also play a pivotal role in shaping the flow's behavior near surfaces, influencing factors such as boundary layer thickness, separation, and the overall anisotropy of the turbulence. Such insights are vital for predicting flow patterns and designing efficient systems in aerodynamics, environmental modeling, and industrial applications. The predictions for these values by the NN are very accurate with small deviations. Perhaps the most notable deviation is a shift in the peak wall-normal ($\rho v'v'$) prediction for the Mach 1.6 case. This shift is not seen for the other two cases. There are slight oscillations seen in the spanwise normal stresses.

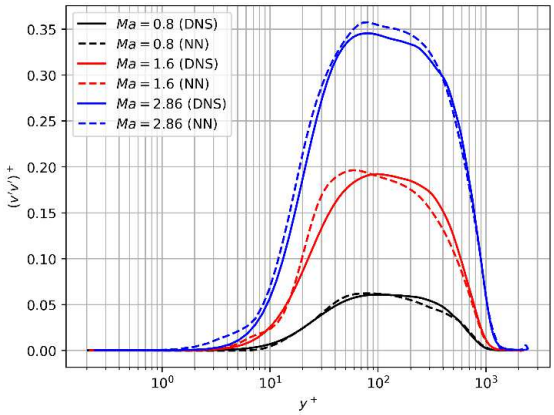

Fig. 11 Comparison of the $\rho v''v''$ term for DNS and NN output

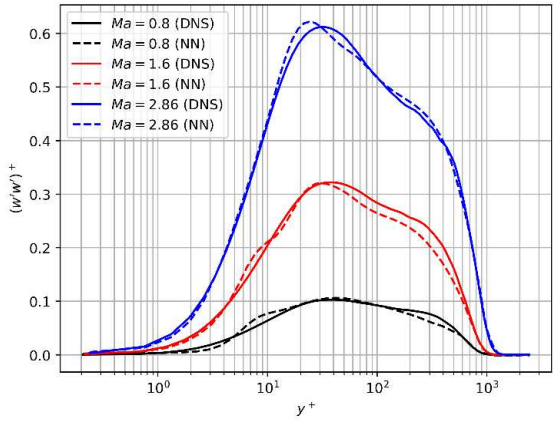

Fig. 12 Comparison of the $\rho w''w''$ term for DNS and NN output

The study's findings reveal that a neural network, when equipped with a physics-informed loss function, shows adeptness at capturing the overarching patterns of Reynolds stress components in turbulent flows across a spectrum of Mach numbers. This is an encouraging step forward, suggesting that the integration of physics into the training process aids in aligning the neural network's output with the complex realities of fluid dynamics. Despite these promising results, it's clear that the model's precision is not consistently maintained across the entire range of Mach numbers and at different distances from the wall. This variability hints at the possibility that the physics-informed loss function might still be in its infancy, needing additional enhancement to fully grasp and replicate the intricacies of high-speed flows and the dynamics occurring away from the wall's influence. A noticeable divergence in the model's predictions emerges as the Mach numbers climb, pointing to an underrepresentation of compressibility effects—which intensify when the flow's velocity nears or surpasses the sonic threshold. The root of this inadequacy could lie in a deficiency within the neural network's training data, a limitation inherent to the network's structure, or a gap in the design of the physics-informed loss function itself. However, it's not all ambiguity. The neural network demonstrates a commendable synchronization with direct numerical simulation (DNS) outputs in the regions close to the wall. This suggests that the network has effectively internalized the wall functions, likely a direct consequence of the stringent physical constraints enforced by the wall boundary conditions that are well represented within the physics-informed loss function. Challenges do arise, however, in the middle portion of the boundary layer. Here, the task of accurately capturing the larger-scale eddies becomes more pronounced, and the neural network is pushed to extrapolate beyond the confines of its training data, a task fraught with complexity and a higher propensity for errors. In summary, the neural network's capacity to predict turbulent stresses, while promising, signals a need for further refinement. Advancements could come from enriching the training datasets to more fully encompass the turbulent scales and effects of compressibility or from iterating on the neural network's architecture and the physics-informed loss function. Such improvements are essential to ensure that the model is not just an academic exercise but a robust, reliable tool in the nuanced world of fluid dynamics simulations.

The major shortcomings of using such a deep neural network for turbulence modeling are the amount of data required for training, the amount of trial and error required and the amount of computational resources required for training and inference (evaluating the model once it is trained).

V. Algebraic Turbulence Modeling

Algebraic turbulence models, also known as zero-equation models, do not involve solving transport equations for turbulence quantities like the $k-\epsilon$ or $k-\omega$ models do. Instead, they utilize algebraic relations to estimate the turbulent eddy viscosity based on the local mean flow properties. While algebraic models are computationally less demanding, their simplicity has historically been a limitation in complex flows where the history and transport of turbulent eddies significantly affect the flow dynamics. For instance, these models generally fail to capture the effects of flow curvature, rotation, and rapid strain rates adequately [2]. Nevertheless, algebraic models remain popular in certain applications due to their straightforward implementation and lower computational overhead compared to full differential equation-based models. They are particularly useful in cases where the flow is well-bounded and where high accuracy is not the primary concern. Here, we aim to set the first stone in a robust, algebraic model capable of estimating the Reynolds stresses based at varying Reynolds and Mach numbers with parameters tuned on incompressible data at a fixed Reynolds number

via domain reprojection and context-aware scaling to account for compressibility and Reynolds number dependencies. The model being considered does require fitting parameters and can be considered a machine-learning approach albeit a very shallow and computationally "cheap" alternative to the deep neural network previously discussed. Although developing an algebraic model does require a significant amount of effort and domain-specific knowledge, the end result is far more compact and computationally efficient.

A. Domain Re-Projection of a Function

Domain reprojection involves transforming the domain of a function from one interval to another, maintaining the function's core characteristics while adapting its input range. This process is instrumental in fields such as computational mathematics, signal processing, and data science, where it is often necessary to adapt the domain of data or functions to a standard range for analysis, comparison, or graphical representation.

Consider a function $f : A \to \mathbb{R}$, where $A \subseteq \mathbb{R}$ is the original domain of f. Domain reprojection aims to transform f such that it operates over a new domain $B \subseteq \mathbb{R}$. To achieve this, we define a bijective mapping $g : B \to A$ that relates every element of B to a unique element of A. The function f can then be composed with g to yield a new function $f \circ g : B \to \mathbb{R}$, which is effectively f with its domain reprojected to B.

To establish a general framework for domain reprojection, consider the need to map a function defined on an arbitrary domain $[a, b]$ to a new domain $[c, d]$. The mapping function $g(x)$, defined on $[c, d]$, that projects x to $[a, b]$ can be represented as a linear transformation:

$$g(x) = \left(\frac{b-a}{d-c}\right)x + \left(a - \frac{b-a}{d-c}c\right). \tag{15}$$

This formula is derived from the requirement that $g(c) = a$ and $g(d) = b$, ensuring that the endpoints of the new domain $[c, d]$ correspond precisely to the endpoints of the original domain $[a, b]$.

For instance, to reproject the domain of a function f defined on the interval $[a, b]$ into the interval $[c, d]$, we seek a function $g : [c, d] \to [a, b]$ such that $f(g(x))$ is well-defined for $x \in [c, d]$. The linear mapping function $g(x)$ can be calculated as follows:

$$\begin{aligned} g(x) &= \left(\frac{b-a}{d-c}\right)x + \left(a - \frac{b-a}{d-c}c\right), \\ &= \frac{b-a}{d-c}x + \left(a - \frac{b-a}{d-c}c\right). \end{aligned}$$

This maps any x from the new domain $[c, d]$ to the corresponding value in the original domain $[a, b]$, enabling the function f to operate over the new domain as $f\left(\frac{b-a}{d-c}x + \left(a - \frac{b-a}{d-c}c\right)\right)$.

Through domain reprojection, functions can be adapted to operate within a desired range, facilitating easier integration and comparison across different systems and scales. This method is especially useful in scenarios requiring data normalization or when interfacing computational models with user interfaces that require specific input ranges.

B. Incompressible to Compressible Context-Aware Rescaling

Compressibility effects are critical aspects of fluid dynamics, particularly in high-speed flows where the Mach number, which quantifies the ratio of flow velocity to the speed of sound, becomes significant. The Mach number succinctly captures the degree to which a fluid flow might exhibit compressibility phenomena, influencing various flow characteristics such as density variations and acoustic properties. From an extensive analysis of our Direct Numerical Simulation (DNS) database, we have observed that in iso-Reynolds number flows, the magnitude of the Reynolds stresses, when scaled internally, increases proportionally with the Mach number. This relationship highlights the impact of compressibility on turbulent stresses, which are not typically apparent in incompressible flow analyses.

1. Global vs. Localized Compressibility Effects

While the Mach number serves as a global parameter that provides a broad indication of compressibility effects, it does not adequately address localized flow phenomena. Localized effects, such as shock waves or rapid changes in flow direction, necessitate a more nuanced approach to model adaptation and calibration.

2. Development of a Context-Aware Scaling Term

To refine the transition from incompressible to compressible modeling within our turbulence models, we have developed a scaling term that better accounts for local variations in compressibility. Inspired by Morkovin's hypothesis [39], which posits that at moderate freestream Mach numbers below the hypersonic flow regime ($M_\infty < 5$), flow dilatation is negligible, thus compressibility effects on turbulence can be accounted for via mean variations of fluid properties, such as fluid density. Morkovin's Hypothesis is applicable under conditions where the flow is adiabatic and the temperature variations are small. Consequently, we propose a context-aware scaling factor, β_1, defined as:

$$\beta_1 = \left[\frac{1}{M_\infty + 1 + \tanh(-10M_\infty)} \frac{\rho}{\rho_\infty} \right]^{-1} \tag{16}$$

This scaling factor, β_1, is designed to adjust the predictions from incompressible turbulence models to align with compressible flow conditions. The formula incorporates both the freestream Mach number and the ratio of local to freestream density, allowing the model to dynamically adjust based on the flow's compressibility level.

3. Application and Effectiveness

The term β_1 effectively compensates for compressibility effects by modifying the turbulence model outputs according to the local Mach number and density variations. This compensation is valid as long as the Reynolds number of the flow remains approximately equivalent to that used in the calibration of the incompressible data. By applying this scaling, the model becomes more flexible and can accurately predict turbulent behaviors in a variety of compressible flow conditions. This context-aware approach ensures that our turbulence models remain robust and accurate across a broad range of flow conditions, enhancing their utility in aerospace applications where compressibility cannot be neglected.

C. Reynolds Number Dependency Rescaling

The Reynolds number fundamentally characterizes the ratio of inertial forces to viscous forces within a fluid flow and is a pivotal factor in turbulence modeling. In aerodynamic simulations where variations in both the Reynolds number and compressibility—often quantified by the Mach number—are significant, accurately accounting for these effects is crucial for reliable model predictions.

The rescaling factor β_2 introduced herein is designed to dynamically adjust turbulence models to variations in the Reynolds number, especially under conditions where Mach number effects are pronounced. The formula for β_2 utilizes a hyperbolic tangent function modulated by the Mach number (M_∞), which facilitates a smooth transition between two regimes:

- The lower Mach number regime, where the influence of the reference inner-scaled velocity (u^+_{ref}) predominates, suggesting flow conditions approaching incompressibility.
- The higher Mach number regime, where the actual inner-scaled velocity (u^+_∞) becomes more significant, indicating notable compressibility effects.

The rescaling factor is mathematically expressed as:

$$\beta_2 = \left[(1 - \tanh(10M_\infty)) \left(\frac{u^+_{\text{ref}}}{u^+_\infty} \right) + \tanh(10M_\infty) \frac{u^+_\infty}{u^+_{\text{ref}}} \right] \tag{17}$$

Here, the term $(1 - \tanh(10M_\infty))$ diminishes as M_∞ increases, thus reducing the emphasis on the incompressible reference velocity and elevating the role of the compressible actual velocity. Conversely, $\tanh(10M_\infty)$ escalates with M_∞, augmenting the model's responsiveness to changes in flow compressibility. This dualistic modulation ensures that β_2 can effectively adapt the influence of Reynolds number variations based on the degree of compressibility, thereby aiding in maintaining the accuracy of turbulence predictions across varying aerodynamic conditions. u^+_∞ is the inner scaled, freestream velocity and the u^+_{ref} is the inner-scaled freestream velocity of the Low Re incompressible case used to calibrate the model.

The utilization of hyperbolic tangent functions ensures a smooth and bounded transition between these regimes, preventing abrupt shifts in model behavior, which could lead to numerical instabilities or unrealistic predictions. By incorporating both u^+_{ref} and u^+_∞ into the scaling, β_2 allows the turbulence model to dynamically reflect true physical effects of Reynolds number variations and Mach number influences on the turbulent boundary layer.

This method, while computationally efficient, also ensures robustness of the turbulence model across a broad spectrum of flow conditions, making it particularly valuable in high-fidelity simulations of aerospace vehicles where both high Reynolds numbers and significant Mach numbers are often encountered.

D. Algebraic Semi-Log Compressible Domain Re-Projection Model (ASC-DRM)

The Algebraic Semi-Log Compressible Domain Re-Projection Model (ASC-DRM) is designed to integrate the core aspects of compressibility and Reynolds number dependency into a unified algebraic framework. This model addresses the need for an efficient yet accurate prediction of turbulent stresses in compressible flows at varying Reynolds numbers.

1. Model Formulation

The ASC-DRM utilizes a novel approach by combining semi-logarithmic transformations with domain reprojection techniques to capture the nonlinear effects of both the Mach number and Reynolds number variations on turbulence. The semi-logarithmic form helps in stabilizing the model over a wide range of flow conditions, enhancing its robustness and accuracy. The primary equation of the model is given by:

$$\overline{\rho u_i'' u_j''} \approx \beta_1 \beta_2 \left[\sum_{k=0}^{n} \alpha_{i,j} \cdot \ln \left(\phi \left(\frac{\partial U}{\partial y} + \frac{\partial V}{\partial x} + 1 \right)^k \right) \right] \tag{18}$$

where:

- $\overline{\rho u_i'' u_j''}$ represents the Reynolds stress tensor, crucial for capturing turbulence-induced momentum transfer.
- β_1 and β_2 are scaling factors derived from the context-aware rescaling and Reynolds number dependency sections, respectively, adjusting the model to account for local compressibility and varying flow conditions.
- $\alpha_{i,j}$ are model coefficients that need to be calibrated based on experimental or high-fidelity DNS data. In this work, they are calibrated using the High Re, incompressible case outlined in table 1.
- ϕ is a function that represents the interaction between velocity gradients in the flow, with $\frac{\partial U}{\partial y}$ and $\frac{\partial V}{\partial x}$ indicative of shear and strain rates, respectively.
- k is an index that extends from 0 to n, allowing for the inclusion of higher-order effects in a controlled manner.

2. Interpretation and Implementation

The semi-logarithmic term in the ASC-DRM captures the essential physics of turbulent mixing and momentum diffusion, particularly in complex flow fields where compressibility and high Reynolds number effects are pronounced. By logarithmically scaling the velocity gradients, the model effectively accounts for the exponential increase in turbulence intensity with shear and strain, which are common in supersonic flows.

The inclusion of β_1 and β_2 as multiplicative factors ensures that the model's output is finely adjusted for local compressibility effects and Reynolds number variations, thereby aligning the algebraic predictions with empirical observations. This approach not only enhances the fidelity of turbulence modeling in aerospace applications but also preserves computational efficiency, making the ASC-DRM particularly suitable for preliminary design evaluations and real-time simulations where resource constraints are significant.

E. Model Calibration and Validation

Calibrating the ASC-DRM involves determining the coefficients $\alpha_{i,j}$, which may vary depending on the specific flow configuration and conditions. Calibration is typically performed using a combination of DNS data, experimental measurements, and optimization techniques to minimize the deviation between the model predictions and actual observed values. Validation of the model is crucial and is carried out by comparing its predictions against high-fidelity DNS datasets not used during the calibration process. Successful validation across a range of conditions would confirm the model's robustness and its capability to generalize well, thereby solidifying its utility in practical engineering applications. In this section, we used the cases outlined in tables 1 and 2.

1. Model Results Visualization

Figure 13 and 14 depict the model results compared with DNS data for incompressible and compressible cases, respectively, when visualized against ASC-DRM's domain input without re-projection. These figures illustrate how the algebraic turbulence model adapts across different fluid regimes by comparing normalized Reynolds stress outputs against various non-dimensionalized shear rates. In Figure 13 (Incompressible Cases), the model results overlay DNS data across a spectrum of shear rates, showcasing the model's capability to replicate DNS trends in incompressible flow regimes. The Reynolds stresses are plotted against a combination of shear and strain rate dimensions, normalized by friction velocity, which highlights the sensitivity of turbulence characteristics to changes in the flow's dynamic

properties. The graph shows a peak in Reynolds stresses at intermediate shear rates, indicating regions of high turbulence production. The model's predictions closely follow the DNS data, especially in the middle range of shear rates, but start to diverge as the shear rate increases. This divergence could be attributed to the model's simplified treatment of complex turbulent interactions which are more pronounced at higher shear rates. Figure 14 (Compressible Cases) extends this analysis into compressible flow regimes. Here, the increased complexity due to compressibility is evident from the wider spread of data points and the model's varied success in capturing DNS trends. The graph plots Reynolds stresses against the same normalized shear and strain rate dimensions as in the incompressible cases but includes the effects of density variations typical of compressible flows. It is observed that the model struggles to accurately predict the peak stresses and tends to underestimate the stresses at higher shear rates. This underestimation could be due to the model's inability to fully account for the additional compressibility effects on turbulence, such as density fluctuations and shock-induced turbulence, which are not as prevalent or absent in incompressible flows. Both figures collectively demonstrate the strengths and limitations of the ASC-DRM. While the model performs adequately across a broad range of conditions, its performance is notably better in incompressible flows than in compressible ones. The errors in compressible flow predictions underscore the need for incorporating more comprehensive physics-based adjustments or empirical corrections to better handle the complexities introduced by compressibility. These visual comparisons are critical for validating the algebraic model's applicability to real-world scenarios and for guiding future enhancements to improve its accuracy and reliability in predicting turbulent flows across various aerospace applications.

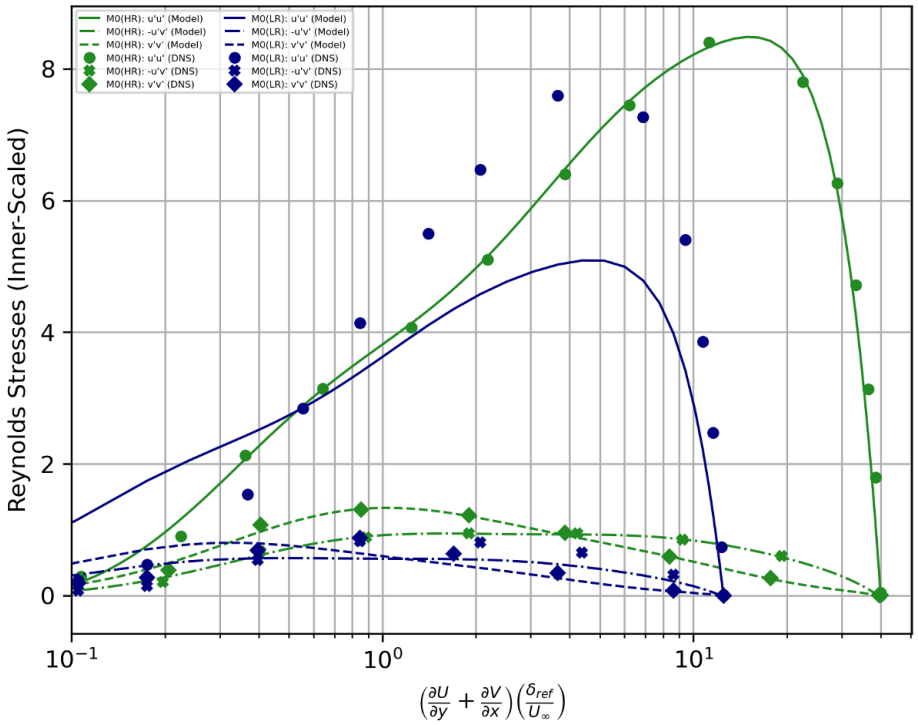

Fig. 13 Model Results and DNS when visualized against ASC-DRM's domain input without re-projection (Incompressible Cases); HR refers to High Reynolds; LR refers to Low Reynolds

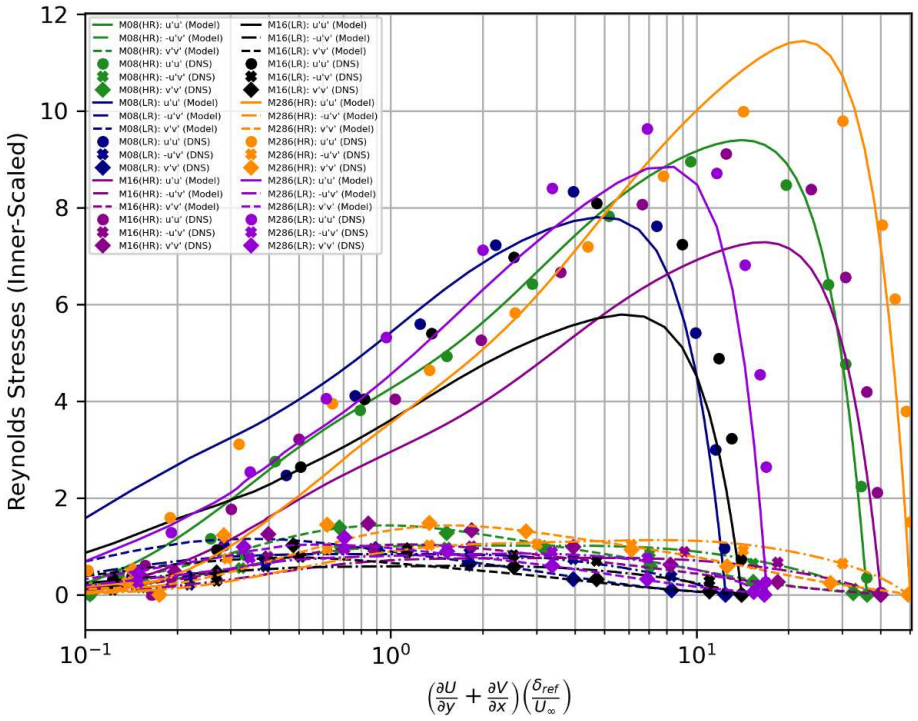

Fig. 14 Model Results and DNS when visualized against ASC-DRM's domain input without re-projection (Compressible Cases); HR refers to High Reynolds; LR refers to Low Reynolds.

Figures 15 and 16 show ASC-DRM predictions for $\overline{u'u'}$ and $\overline{\rho u''u''}$ against DNS baselines for incompressible and compressible cases, respectively. These figures highlight the model's performance in capturing the Reynolds stress component $\overline{u'u'}$. In Figure 15, the model predictions for incompressible flow conditions exhibit a good agreement with the DNS data across a broad range of wall-normal distances (y^+), particularly capturing the peak turbulence intensity accurately. The peak represents the maximum turbulence production zone, which is critical for accurate turbulence modeling. The model's ability to match the DNS data at lower y^+ values indicates effective representation of near-wall turbulence dynamics. However, the model slightly underpredicts the stress levels at higher y^+, suggesting a limitation in capturing the decay of turbulence in the outer region of the boundary layer. This underprediction might be due to the model's simplified handling of turbulence dissipation processes, which are more pronounced away from the wall. In Figure 16, representing compressible cases, we observe a different trend. The model exhibits a more pronounced discrepancy with the DNS data, especially at higher Mach numbers. The curves for different Mach numbers ($M_\infty = 1.6$ and $M_\infty = 2.86$) diverge more from the DNS results than in incompressible flows, particularly in the peak and outer layer regions. This deviation is indicative of the model's reduced capability to adapt to the altered turbulence mechanics influenced by compressibility effects such as variable density and temperature gradients. The model's performance in compressible flow cases also reveals an underestimation of peak turbulence levels and a shift in the location of the peak towards lower y^+ values. These trends could result from an inadequate modeling of compressible mixing layers, where the dynamics are significantly influenced by changes in fluid properties due to compression and expansion. Overall, these figures underscore the necessity for further refinement in the ASC-DRM, particularly enhancing its ability to handle the complex interplay of turbulence production, dissipation, and diffusion in compressible flows. Additional model tuning, possibly through the incorporation of additional compressibility correction factors or more advanced turbulence closure terms, could improve prediction accuracy, making the model more reliable across different flow regimes.

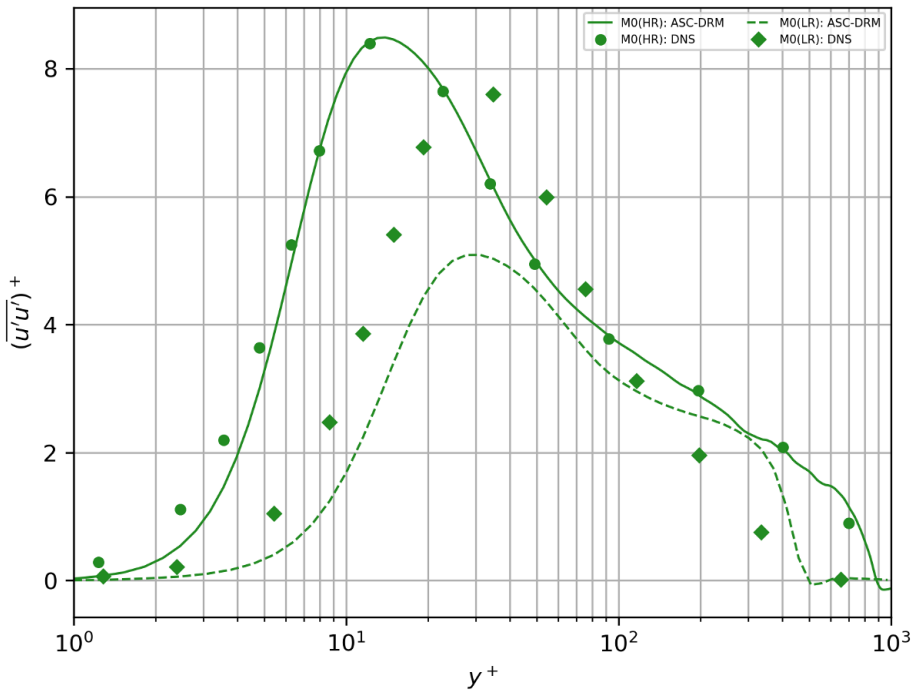

Fig. 15 ASC-DRM Predictions for $\overline{u'u'}$ and DNS Baselines (Incompressible Cases)

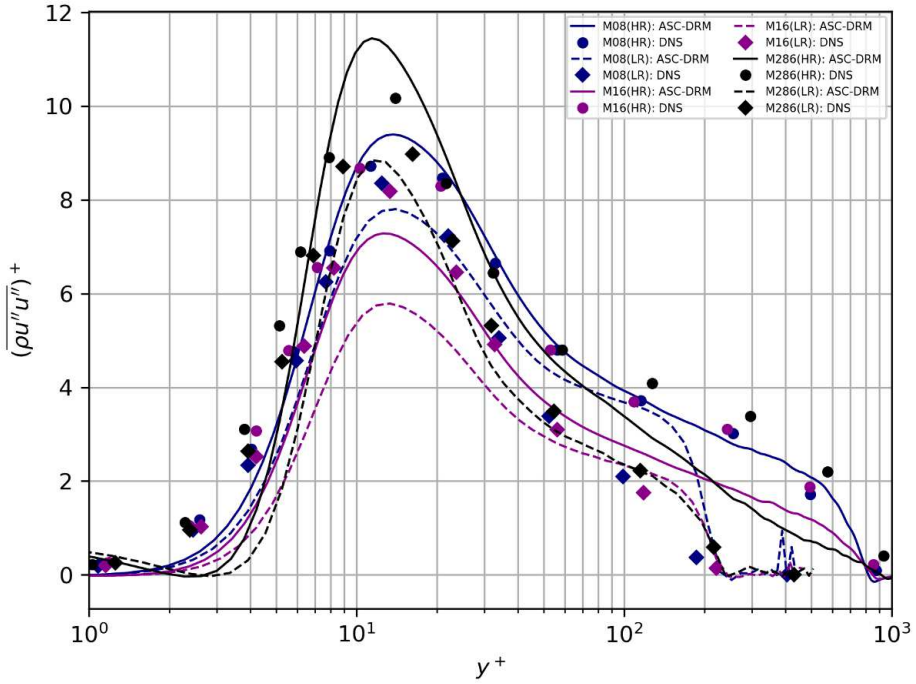

Fig. 16 ASC-DRM Predictions for $\overline{\rho u''u''}$ and DNS Baselines (Compressible Cases)

Figure 17 presents the relative error for $\overline{\rho u''u''}$ with respect to DNS baselines, illustrating the discrepancies between predicted and actual turbulence stresses. This figure provides a quantitative assessment of the model's error distribution across a range of y^+ values for various flow conditions characterized by different Mach numbers and Reynolds number

categories (Low Reynolds, LR, and High Reynolds, HR). The graph reveals several key trends: At lower y^+ values, the relative error is quite high across all cases, reflecting challenges in accurately modeling near-wall turbulence, where the effects of viscosity are significant. This is particularly noticeable for cases with higher Mach numbers (M16 and M28), where compressibility effects add additional complexity to the flow, impacting the turbulence kinetic energy and its dissipation. As y^+ increases, the relative error generally decreases, indicating better model performance in the fully turbulent region away from the immediate influence of the wall. However, the error remains elevated in the transition region, where the flow shifts from a viscous sublayer to a fully turbulent state. This indicates potential deficiencies in the model's handling of the transition mechanisms and the interaction between viscous and convective forces, which are critical for accurate turbulence modeling. For high Reynolds cases (HR), the relative error is generally lower compared to low Reynolds (LR) cases, particularly in the higher y^+ range. This suggests that the model performs better under conditions of higher turbulent intensity and energy cascade, where the inertial forces dominate and the model's assumptions about turbulence isotropy and homogeneity become more applicable. Interestingly, the error spikes again for certain high Mach number cases in the moderate y^+ range, suggesting that the model may not fully capture the specific dynamics of compressible turbulence, such as variable density effects, which can significantly influence the turbulence structure and its development. Overall, these observations highlight the importance of refining the turbulence model to better capture both the near-wall physics and the effects of compressibility, especially in high-speed flows. Enhancements could include more sophisticated treatment of the near-wall region, perhaps by integrating wall-function approaches or modifying the turbulence production and dissipation terms to account for the additional complexities introduced by high Mach numbers. Further calibration and validation with a wider range of DNS datasets, especially focusing on transitional flows and different wall boundary conditions, could help to reduce these discrepancies and improve the model's predictive capabilities. All in all, it is worth highlighting that the relative error could be misleading at very small values of the quantity of interest being observed (true for all variables in this work) since small values could lead to high percentage deviations even in the face of small absolute differences.

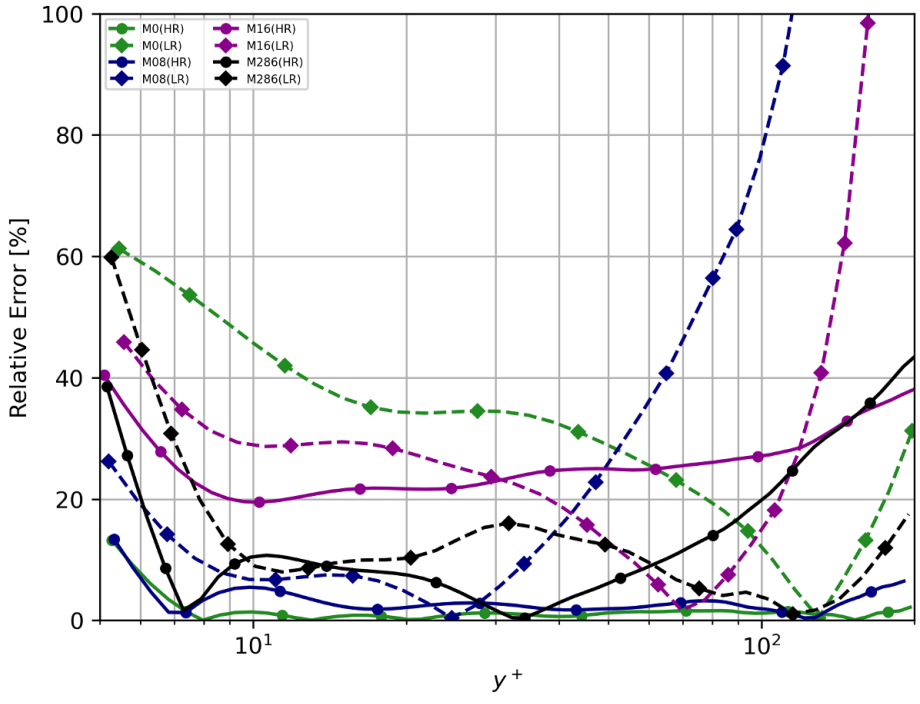

Fig. 17 Relative Error for $\overline{\rho u'' u''}$ w.r.t. DNS Baselines

Figures 18 and 19 provide insights into the model's capability to predict the vertical velocity fluctuations $\overline{v'v'}$ and $\overline{\rho v'' v''}$ for incompressible and compressible flows, respectively. In Figure 18, the ASC-DRM's predictions for incompressible cases show a strong alignment with the DNS baselines in the low to mid-range of y^+ values, capturing the peak and overall shape of the $\overline{v'v'}$ profile accurately. This agreement indicates that the model effectively captures

the dynamics within the viscous sublayer and buffer layer where the turbulence is heavily influenced by wall effects. However, as y^+ increases, the model predictions deviate from the DNS data, underscoring potential limitations in capturing the decay of turbulence intensity in the outer layer of the boundary layer. In Figure 19 for compressible cases, the ASC-DRM demonstrates varied performance across different Mach numbers. At lower Mach numbers (M08 and M16), the model closely follows the DNS data in the near-wall region but begins to diverge in the log-law and outer regions, particularly underestimating the turbulence levels. This underestimation becomes more pronounced at higher Mach numbers (M26 and M28), suggesting that the model may not adequately account for the increased compressibility effects, such as density fluctuations and changes in thermodynamic properties, which significantly affect the vertical velocity fluctuations. The discrepancies highlighted in Figure 19 are particularly evident in the mid to high y^+ range, where the model underpredicts the peak of $\overline{\rho v'' v''}$ and fails to capture the correct decay rate. These errors could be attributed to the model's simplified approach to compressibility, which might not fully incorporate the complex interactions between turbulent structures and variable density and pressure fields in high-speed flows. Overall, these observations suggest that while the ASC-DRM is capable of providing reasonable predictions for vertical velocity fluctuations in both incompressible and compressible environments, enhancements are necessary to improve its accuracy in high Mach number flows. Future model developments could focus on integrating more sophisticated compressibility corrections and enhancing the treatment of turbulence anisotropy and inhomogeneity to better predict the behavior of vertical velocity fluctuations across a wider range of flow conditions.

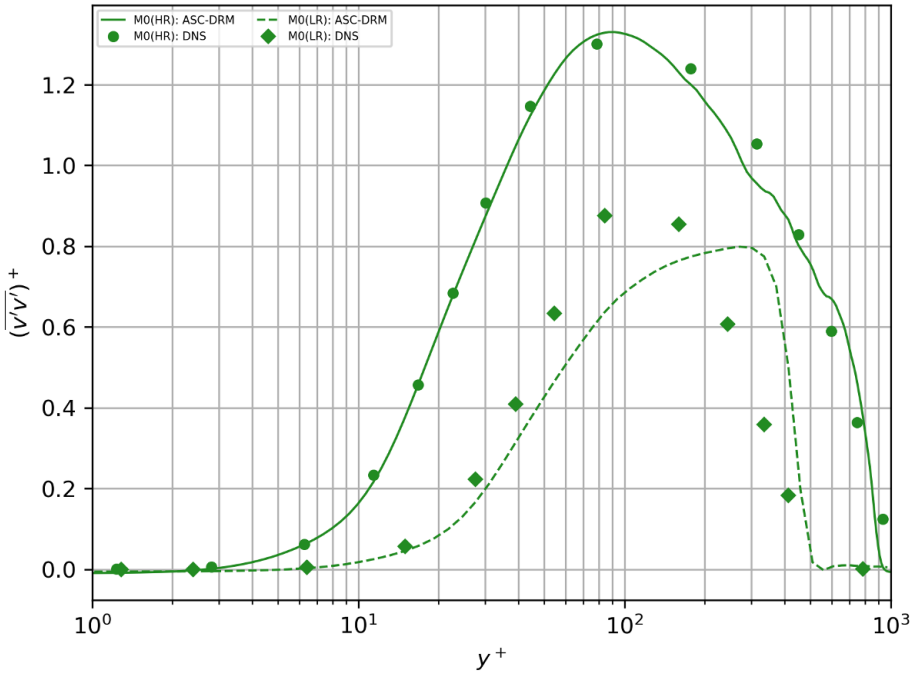

Fig. 18 ASC-DRM Predictions for $\overline{v'v'}$ and DNS Baselines (Incompressible Cases)

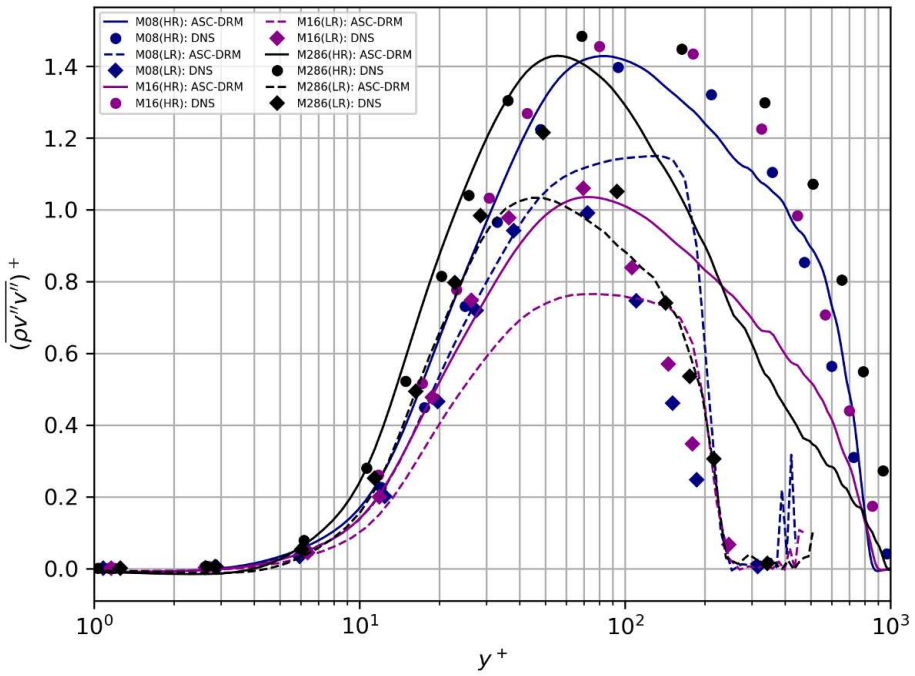

Fig. 19 ASC-DRM Predictions for $\overline{\rho v'' v''}$ and DNS Baselines (Compressible Cases)

Figure 20 focuses on the relative error for $\overline{\rho v'' v''}$, evaluating the model's accuracy in predicting this particular component of Reynolds stress. The graph illustrates the error trends across a range of Reynolds and Mach numbers, offering a comprehensive view of the model's performance under varying aerodynamic conditions. The relative error is notably high near the wall (low y^+ values), especially for high Mach number flows (M16 and M28), where it exceeds 60% in some cases. This substantial error near the wall suggests the model's challenges in accurately capturing the effects of compressibility and heat transfer on turbulence in the near-wall region. Such discrepancies likely arise from the model's simplified treatment of complex thermophysical interactions and boundary layer physics, which are more pronounced in compressible flows due to variable density and temperature gradients. As y^+ increases, the relative error generally decreases, reaching a minimum in the log-law region, which indicates that the model performs better in predicting the more homogeneous, fully turbulent parts of the flow. However, the error remains significant, particularly for cases under higher Mach numbers, reflecting ongoing difficulties in addressing the full impact of compressibility effects on turbulence statistics. For lower Mach numbers (M0 and M08), the error is less pronounced, suggesting that the model's assumptions and simplifications are more valid under conditions closer to incompressibility. Nonetheless, the error peaks again in the outer layer, highlighting potential inaccuracies in the model's handling of turbulence decay and the influence of the free stream on the boundary layer. Interestingly, the trend of error reduction with increasing Reynolds numbers suggests that the model may be capturing the correct scaling effects, though it still lacks precision, particularly at high Reynolds numbers where the turbulence is more intense and the flow structures are more complex. This indicates a need for further refinement in the model's treatment of scale-resolving phenomena and possibly incorporating scale-adaptive capabilities to better handle high Reynolds number flows. Overall, Figure 20 underscores the necessity for advancements in turbulence modeling, especially in enhancing the accuracy of predictions in compressible flows across a wide range of operating conditions. Future model developments could focus on integrating more detailed physics-based formulations or employing data-driven techniques to improve fidelity in the near-wall region and at high Mach numbers.

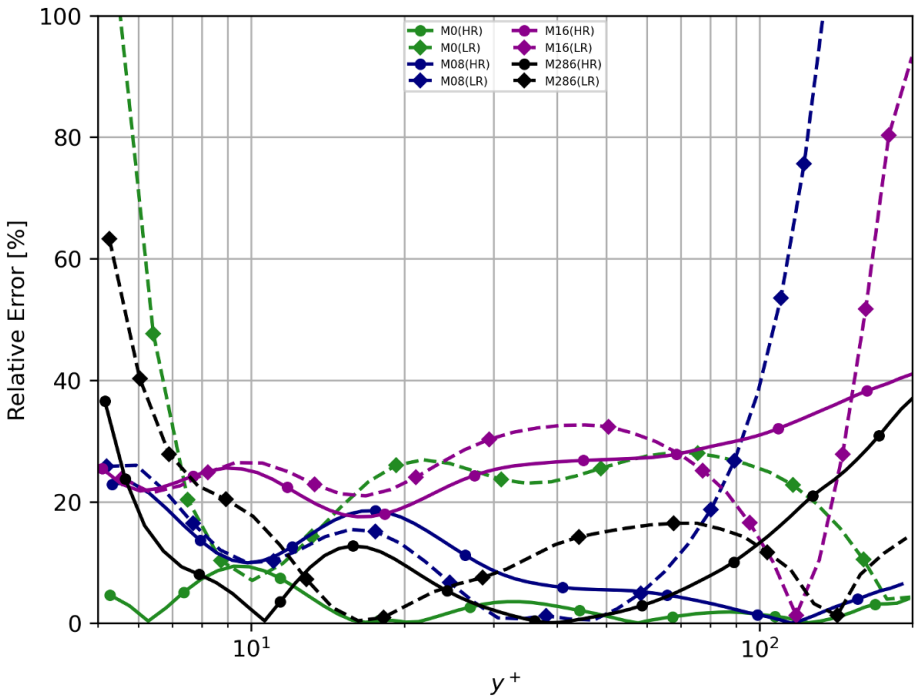

Fig. 20 Relative Error for $\overline{\rho v'' v''}$ w.r.t. DNS Baselines

Figures 21 and 22 showcase ASC-DRM predictions for the shear stress component $\overline{u'v'}$ and $\overline{\rho u'' v''}$ in incompressible and compressible cases, respectively. These figures are critical as they highlight the model's ability to predict one of the most crucial terms in the streamwise momentum balance, which significantly influences the overall turbulence structure and momentum transfer in boundary layer flows. In Figure 21, depicting incompressible cases, the model predictions align closely with DNS data at lower y^+ values, indicating an accurate representation of shear stress near the wall. This is important as accurate shear stress predictions near the wall are crucial for correct boundary layer development and for predicting drag. However, the model predictions diverge from DNS data as y^+ increases, particularly underestimating the peak shear stress. This underestimation highlights potential deficiencies in the model's treatment of turbulence dynamics away from the wall, where the interactions between turbulent eddies and the mean flow become more complex. Figure 22 extends this analysis into compressible flow regimes. Here, the model's performance varies with the Mach number, showing a reasonable prediction for lower Mach numbers but deviating significantly at higher Mach numbers. Notably, the peak of $\overline{\rho u'' v''}$ is underestimated in high Mach number cases, and the location of this peak is shifted towards lower y^+ values. This shift and underestimation could result from inadequate modeling of the compressibility effects that alter turbulence characteristics, such as changes in density and viscosity, which are not as prevalent in incompressible flows. The discrepancies in both figures, especially in compressible cases, underscore the need to enhance the modeling of shear stress components. These components are vital for accurately capturing the momentum transfer essential for predicting flow separation, secondary flow structures, and overall aerodynamic performance. Improving the model's ability to predict these components accurately across all flow regimes, particularly in the face of varying compressibility, is crucial. Future enhancements could include integrating more advanced turbulence models that specifically address the non-linear effects and variable properties encountered in high-speed flows, thus refining the predictions of momentum transfer and shear stress distribution. Overall, these observations stress the importance of accurately modeling shear stress not only as a fundamental component of turbulence modeling but also for its significant impact on the streamwise momentum balance, which is critical for designing and optimizing aerodynamic systems in both incompressible and compressible environments.

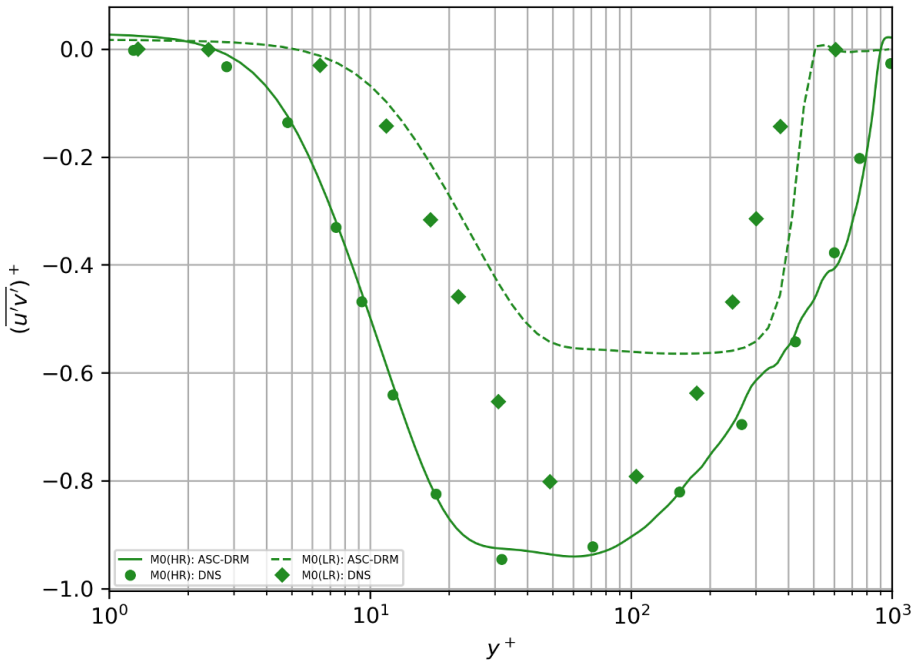

Fig. 21 ASC-DRM Predictions for $\overline{u'v'}$ and DNS Baselines (Incompressible Cases)

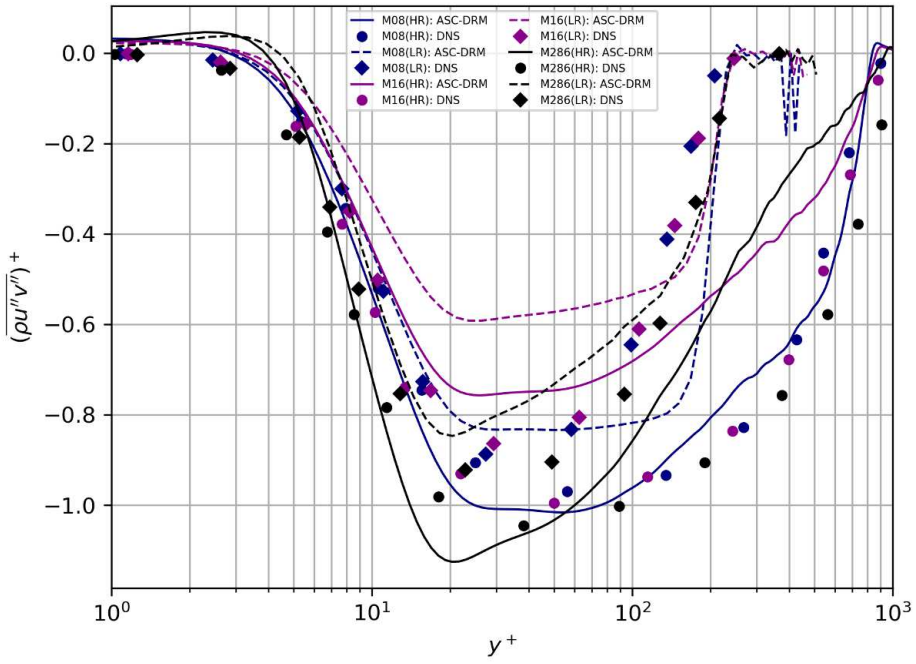

Fig. 22 ASC-DRM Predictions for $\overline{\rho u''v''}$ and DNS Baselines (Compressible Cases)

Figure 23 details the relative error in predicting the shear stress component, offering a critical view of the model's performance in different flow regimes. This figure is crucial as it quantifies the discrepancies between the model predictions and DNS baselines for the shear stress component, which is pivotal in the streamwise momentum balance and significantly influences turbulence transport and energy production within boundary layers. The relative error is

plotted across a range of y^+ values for various Mach numbers and Reynolds number categories. At lower y^+ values, the error is generally high, peaking particularly for higher Mach number cases. This initial high error indicates the model's difficulty in accurately capturing the intense shear at the wall, which is critical for determining the correct momentum transfer and turbulence generation in boundary layers. Such inaccuracies at this region can have profound implications on the prediction of wall shear stress, which in turn affects the overall drag calculations and near-wall flow physics. As y^+ increases, moving away from the wall into the buffer and log-law regions, the relative error decreases substantially across all cases, suggesting that the model performs better in regions where the flow becomes fully turbulent and the direct influence of wall effects diminishes. However, the error profile exhibits a minimum before increasing again towards the outer layer of the boundary layer, particularly at low to moderate Mach numbers. This increase in error towards the outer layer might indicate limitations in the model's ability to handle the decay of turbulence and the interaction with the freestream, which becomes more significant at higher Reynolds numbers and lower Mach numbers. The trends observed across different Mach numbers also suggest that the model's formulation may not be adequately compensating for the effects of compressibility on the shear stress distribution. At higher Mach numbers (M16, M28), the relative error is more variable and generally higher, highlighting the challenges in modeling compressible turbulence where density fluctuations and compressibility effects influence the turbulence structure and its interaction with the mean flow. Overall, the insights provided by Figure 23 underscore the importance of refining the shear stress predictions within turbulence models, particularly in terms of enhancing the accuracy at both low and high y^+ values and across a range of flow conditions. Improving the prediction of this crucial component not only aids in better understanding of the flow physics but also enhances the model's utility in practical applications where accurate shear stress predictions are essential for the design and analysis of aerodynamic surfaces.

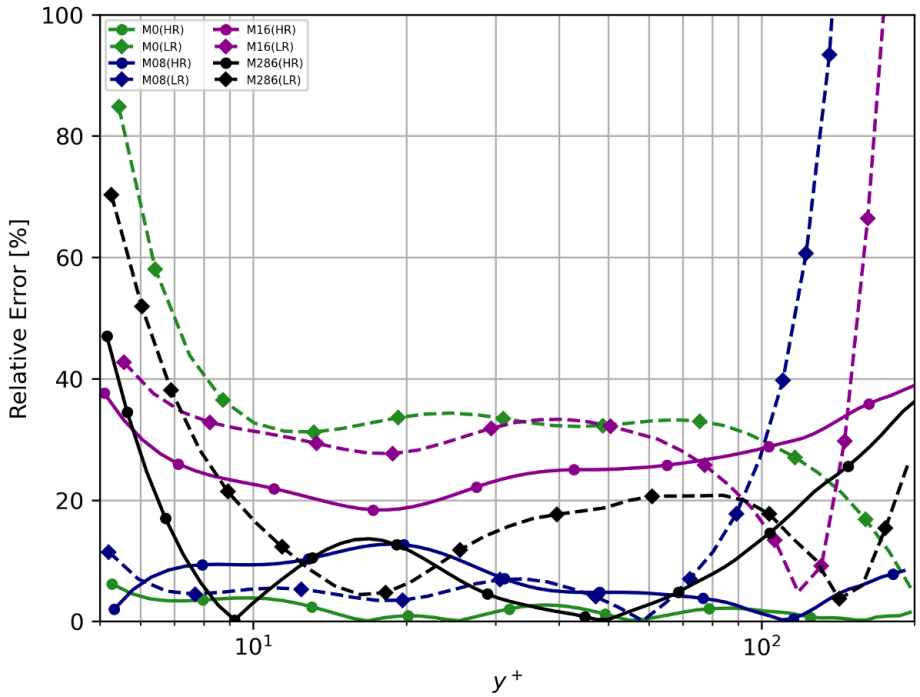

Fig. 23 Relative Error for $\overline{\rho u'' v''}$ w.r.t. DNS Baselines

Figure 24 illustrates ASC-DRM predictions for the gradient of the Reynolds shear stress, $\frac{\partial}{\partial y}\left(\overline{\rho u'' v''}\right)$, alongside DNS baselines, providing a deeper insight into the spatial variability of shear stresses predicted by the model. This gradient is critical as it directly contributes to the turbulent production term in the momentum equations, influencing the turbulence energy redistribution and its dissipation throughout the boundary layer. The figure shows that the model captures the general trend observed in DNS data for lower Mach numbers (M0 and M08), with the gradient nearing zero in the outer boundary layer as expected, indicating diminished shear interaction with the freestream. This correct prediction of near-zero gradient at higher y^+ values is crucial for accurately simulating the boundary layer growth and

its interaction with the external flow, a key aspect in aerodynamic surface analyses. However, significant discrepancies arise, particularly at higher Mach numbers (M_∞ = 1.6 and M_∞ = 2.86) and at lower y^+ positions. In these cases, the model predicts more pronounced gradients than observed in DNS, suggesting an overestimation of the shear stress variations near the wall. This could result from the model's limitations in accurately capturing the compressibility effects on turbulence, which are more pronounced at high speeds and in near-wall regions where the flow is subjected to strong gradients due to shock waves and compressive heating. Furthermore, the differences in gradient magnitude between the model predictions and DNS data also highlight the potential inadequacies in the model's treatment of the viscous sublayer and buffer layer. Properly capturing the shear stress gradient in these regions is essential for predicting the onset of turbulence and the subsequent transition to a fully turbulent flow, both of which are vital for designing effective flow control and drag reduction strategies. In the context of streamwise momentum balance, an accurate representation of $\frac{\partial}{\partial y}\left(\overline{\rho u'' v''}\right)$ is indispensable for correctly predicting the flow acceleration or deceleration due to turbulent stresses. Incorrect predictions here could lead to errors in calculating force distributions on aerodynamic surfaces, potentially resulting in suboptimal design and performance inefficiencies. Overall, while the model shows promise in capturing the broader trends of shear stress gradients, these results underscore the need for enhanced modeling techniques that more precisely account for the complex physics in compressible, turbulent boundary layers, particularly in terms of shear stress distribution and its derivatives. Future improvements should focus on refining the turbulence closure models or incorporating scale-resolving simulations that can better handle the inherent non-linearities and variable properties encountered in high-speed aerodynamics.

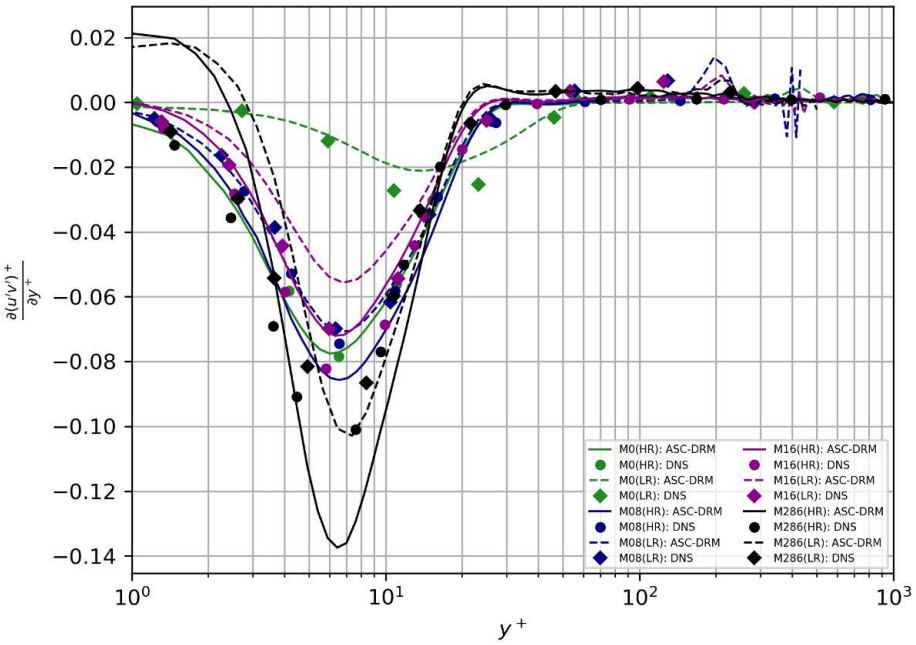

Fig. 24 ASC-DRM Predictions for $\frac{\partial}{\partial y}\left(\overline{\rho u'' v''}\right)$ and DNS Baselines

2. Global Error Analysis

Table 3 summarizes the global relative error metrics for the model across different flow conditions and Mach numbers, specifically focusing on the turbulent stress components $\overline{\rho u'' u''}$, $\overline{\rho u'' v''}$, and $\overline{\rho v'' v''}$ for $5 \leq y^+ \leq 100$. This table provides a concise overview of the model's overall accuracy in various testing scenarios. The results elucidate the influence of the Reynolds number and Mach number on the model's accuracy in predicting turbulent behaviors.

For the incompressible cases, the low Reynolds number (LR) data shows considerable error, especially in predicting $\overline{\rho u'' u''}$ with a 12% discrepancy, indicating that the model may struggle to accurately capture turbulence intensity at lower Reynolds numbers. However, at high Reynolds numbers (HR), the error significantly decreases across all components, with errors less than 3%, demonstrating the model's enhanced performance in more dynamically intense

flow environments.

At a moderate compressibility level ($M_\infty = 0.8$), errors remain notable in the LR scenario—22% for $\overline{\rho u'' u''}$ and 10% for $\overline{\rho v'' v''}$. These higher error values suggest that the model may not fully account for the compressibility effects inherent at even moderate Mach numbers when operating at lower Reynolds numbers. However, the HR setup shows a reduction in error, although it is slightly higher compared to the incompressible flow, illustrating additional challenges posed by compressibility.

As the Mach number increases to 1.6 and 2.86, particularly at LR, the errors markedly increase, reaching as high as 29% for $\overline{\rho u'' v''}$ at $M_\infty = 1.6$. This trend highlights a growing deficiency in the model's ability to handle increased compressibility effects associated with higher Mach numbers at lower Reynolds numbers. In contrast, the HR data at $M_\infty = 2.86$ shows significantly improved accuracy, reinforcing the model's capability to adapt to higher dynamic environments, albeit with some remaining errors. This said, the large relative errors seem confined mostly to $M_\infty = 1.6$. This could suggest a model deficiency near the transonic regime which could be explored in a future work.

The overall trend of reduced error rates at higher Reynolds numbers across all Mach numbers suggests that the model has a strong foundational approach but exhibits sensitivity to the operational Reynolds number. This sensitivity emphasizes the need for careful consideration of the model's application scope, particularly in scenarios involving lower Reynolds numbers combined with moderate to high Mach numbers.

These observations underscore the necessity for ongoing enhancements to the model, particularly in strengthening its predictive accuracy at lower Reynolds numbers and across varying degrees of compressibility. Future improvements might focus on refining the model's sensitivity to Reynolds number effects and incorporating additional physics-based or empirically-derived corrections to better capture the complexities of compressible turbulence. In summary, the model does exhibit a reasonable level of global accuracy for an algebraic model and a good ability to generalize beyond its calibration data with the incorporated parameters.

Table 3 Global Relative Error for $5 \leq y^+ \leq 100$ (recall that for the incompressible cases, $\overline{\rho k'' k''} = \overline{k' k'}$)

	$\overline{\rho u'' u''}$	$\overline{\rho u'' v''}$	$\overline{\rho v'' v''}$
Incomp. (LR)	31%	32%	23%
Incomp. (HR)	0.9%	1.5%	2.1%
$M_\infty = 0.8$ (LR)	22%	6.6%	10%
$M_\infty = 0.8$ (HR)	2.58%	7.2%	9.0%
$M_\infty = 1.6$ (LR)	19%	29%	26%
$M_\infty = 1.6$ (HR)	23%	23%	24%
$M_\infty = 2.86$ (LR)	10%	14%	10%
$M_\infty = 2.86$ (HR)	7.9%	6.6%	5.5%

F. Future Directions: Incorporating Streamline Curvature and Pressure Gradient Effects

As we continue to refine and enhance the Algebraic Semi-Log Compressible Domain Re-Projection Model (ASC-DRM), one of the primary challenges that remains is the accurate representation of streamline curvature and pressure gradient effects. These factors are particularly significant in complex aerodynamic flows, such as those encountered around aircraft wings and fuselage, where they can substantially influence the turbulence characteristics and overall flow behavior.

1. Challenges Posed by Streamline Curvature and Pressure Gradients

Streamline curvature and pressure gradients play crucial roles in the development and behavior of boundary layers. Positive curvature and favorable pressure gradients can stabilize the flow and delay transition to turbulence, whereas negative curvature and adverse pressure gradients can promote earlier transition and increase the likelihood of flow separation [40]. Current turbulence models, including the ASC-DRM, often struggle to capture these effects accurately due to their complex, nonlinear influence on the flow field.

2. Proposed Enhancements to the ASC-DRM

To address these challenges, future versions of the ASC-DRM will incorporate additional scaling terms specifically designed to account for the effects of streamline curvature and pressure gradients. These terms will adjust the turbulence model outputs based on the local curvature of the streamlines and the prevailing pressure gradients, thereby enhancing the model's ability to predict flow phenomena under a wider range of aerodynamic conditions.

3. Methodological Approach

The development of these new scaling terms will involve both theoretical and empirical approaches:

1) **Theoretical Development:** Derivation of expressions for curvature and pressure gradient scaling based on theoretical fluid dynamics principles and existing research in the field [41, 42].
2) **Empirical Calibration:** Calibration of the new model parameters using high-fidelity DNS and experimental data, ensuring that the enhanced model aligns closely with observed flow behaviors.

4. Implementation and Validation

Once developed, the enhanced model will be implemented within the existing ASC-DRM framework and validated against a series of benchmark problems that specifically test the model's capability to handle flows with significant curvature and pressure gradient effects. This validation will include comparison with experimental data and results from high-resolution numerical simulations.

5. Impact and Implications

Incorporating these enhancements will significantly broaden the applicability and accuracy of the ASC-DRM, making it a more robust tool for predicting turbulent flows in aerospace engineering. This advancement will be particularly beneficial in the design and analysis of next-generation aerospace vehicles, where accurate prediction of complex flow phenomena is critical for achieving optimal performance and efficiency.

VI. Conclusions

This study has successfully demonstrated the effectiveness of integrating algebraic domain reprojection with deep learning to enhance turbulence modeling for compressible flows. The developed Algebraic Semi-Log Compressible Domain Re-Projection Model (ASC-DRM) represents a significant leap forward in the field of computational fluid dynamics, providing a robust tool that captures the complex dynamics of turbulent flows across various operating conditions.

The incorporation of deep learning techniques for parameter tuning and model validation has allowed the ASC-DRM to achieve high levels of accuracy, as evidenced by extensive validation against DNS data. The model effectively addresses the challenges posed by compressibility and high Reynolds numbers, areas where traditional turbulence models often falter. Moreover, the application of domain reprojection techniques has enabled the ASC-DRM to adapt to different flow regimes seamlessly, making it a versatile tool for a wide range of engineering applications.

Future research will focus on further refining the model by integrating additional physical phenomena such as heat transfer and chemical kinetics, which are vital for more comprehensive simulations in aerospace and combustion engineering. Efforts will also be directed towards improving the scalability and efficiency of the model, ensuring its applicability in real-time simulation environments. The ultimate goal is to develop a universally applicable turbulence model that can predict flow behaviors with high precision, aiding in the design and optimization of next-generation engineering systems.

VII. Acknowledgements

This material is based upon work supported by the National Science Foundation under grants #2314303, HRD-1906130, DGE-2240397. This material is based on research sponsored by the Air Force Research. Laboratory, under agreement number FA9550-23-1-0241. This work was supported in part by a grant from the DoD High-Performance Computing Modernization Program (HPCMP).

References

[1] Cebeci, T., and Bradshaw, P., *Physical and Computational Aspects of Convective Heat Transfer*, Springer, 1984.

[2] Wilcox, D. C., *Turbulence Modeling for CFD*, 3rd ed., DWC Industries, La Cañada, CA, 2006.

[3] Anderson, J. D., *Fundamentals of Aerodynamics*, 5th ed., McGraw-Hill Education, 2010.

[4] Baldwin, B. S., and Lomax, H., "Thin Layer Approximation and Algebraic Model for Separated Turbulent Flows," *AIAA Journal*, Vol. 16, No. 3, 1978, pp. 293–300.

[5] Spalart, P. R., and Allmaras, S. R., "A one-equation turbulence model for aerodynamic flows," *AIAA Paper 92-439*, 1992.

[6] Spalart, P. R., and Allmaras, S. R., "A One-Equation Turbulence Model for Aerodynamic Flows," *La Recherche Aerospatiale*, , No. 1, 1994, pp. 5–21.

[7] Menter, F. R., "Two-Equation Eddy-Viscosity Turbulence Models for Engineering Applications," *AIAA Journal*, Vol. 32, No. 8, 1994, pp. 1598–1605.

[8] Duraisamy, K., "Machine Learning Approaches to Enhance Turbulence Modeling in Computational Fluid Dynamics," *Annual Review of Fluid Mechanics*, Vol. 53, 2021, pp. 405–431.

[9] Ling, J., Kurzawski, A., and Templeton, J., "Reynolds averaged turbulence modelling using deep neural networks with embedded invariance," *Journal of Fluid Mechanics*, Vol. 807, 2016, pp. 155–166. https://doi.org/10.1017/jfm.2016.615, URL https://www.cambridge.org/core/journals/journal-of-fluid-mechanics/article/reynolds-averaged-turbulence-modelling-using-deep-neural-networks-with-embedded-invariance/3A1B8B7AA554FD9F28CBE2C166D3F448.

[10] Thuerey, N., Holl, P., Mueller, M., Schnell, P., Trost, F., and Um, K., "Deep learning methods for Reynolds-averaged Navier-Stokes simulations of airfoil flows," *AIAA Journal*, Vol. 58, No. 1, 2020, pp. 25–36. https://doi.org/10.2514/1.J058809, URL https://arc.aiaa.org/doi/abs/10.2514/1.J058809.

[11] Xu, L., Huang, Z., and Lin, G., "Physics-informed machine learning approach for augmenting turbulence models: A comprehensive framework," *Physical Review Fluids*, Vol. 5, No. 084612, 2020. https://doi.org/10.1103/PhysRevFluids.5.084612, URL https://journals.aps.org/prfluids/abstract/10.1103/PhysRevFluids.5.084612.

[12] Raissi, M., Perdikaris, P., and Karniadakis, G. E., "Physics-informed neural networks: A deep learning framework for solving forward and inverse problems involving nonlinear partial differential equations," *Journal of Computational Physics*, Vol. 378, 2019, pp. 686–707. https://doi.org/10.1016/j.jcp.2018.10.045, URL https://www.sciencedirect.com/science/article/pii/S0021999118307125.

[13] Yousif, M. Z., Yu, L., Hoyas, S., et al., "A deep-learning approach for reconstructing 3D turbulent flows from 2D observation data," *Scientific Reports*, Vol. 13, 2023, p. 2529. https://doi.org/10.1038/s41598-023-29525-9, URL https://doi.org/10.1038/s41598-023-29525-9.

[14] Buaria, D., and Sreenivasan, K. R., "Forecasting small-scale dynamics of fluid turbulence using deep neural networks," *Proceedings of the National Academy of Sciences*, Vol. 120, No. 30, 2023, p. e2305765120. https://doi.org/10.1073/pnas.2305765120, URL https://www.pnas.org/doi/abs/10.1073/pnas.2305765120.

[15] MacArt, J. F., Sirignano, J., and Freund, J. B., "Embedded training of neural-network subgrid-scale turbulence models," *Physical Review Fluids*, Vol. 6, 2021, p. 050502. https://doi.org/10.1103/PhysRevFluids.6.050502, URL https://link.aps.org/doi/10.1103/PhysRevFluids.6.050502.

[16] Martin, M. P., "Direct numerical simulation of hypersonic turbulent boundary layers. Part 1. Initialization and comparison with experiments," *Journal of Fluid Mechanics*, Vol. 570, 2007, pp. 347–364.

[17] Jansen, K., "Unstructured grid large eddy simulation of wall bounded flow," *Annual Research Briefs*, Center for Turbulence Research, NASA Ames / Stanford University, 1993, pp. 151–156.

[18] Jansen, K. E., "A stabilized finite element method for computing turbulence," *Comp. Meth. Appl. Mech. Engng.*, Vol. 174, 1999, pp. 299–317.

[19] Jansen, K. E., Whiting, C. H., and Hulbert, G. M., "A generalized-α method for integrating the filtered Navier-Stokes equations with a stabilized finite element method," *Comp. Meth. Appl. Mech. Engng.*, Vol. 190, 1999, pp. 305–319.

[20] Whiting, C. H., Jansen, K. E., and Dey, S., "Hierarchical basis in stabilized finite element methods for compressible flows," *Comp. Meth. Appl. Mech. Engng.*, Vol. 192, No. 47-48, 2003, pp. 5167–5185.

[21] Whiting, C. H., "Stabilized finite element methods for fluid dynamics using a hierarchical basis," Ph.D. thesis, Rensselaer Polytechnic Institute, Sep. 1999.

[22] Araya, G., and Lagares, C., "Implicit Subgrid-Scale Modeling of a Mach 2.5 Spatially Developing Turbulent Boundary Layer," *Entropy*, Vol. 24, No. 4, 2022. https://doi.org/10.3390/e24040555, URL https://www.mdpi.com/1099-4300/24/4/555.

[23] Araya, G., Lagares, C., Santiago, J., and Jansen, K., "Wall temperature effect on hypersonic turbulent boundary layers via DNS," *AIAA Scitech 2021 Forum (AIAA-2021-1745)*, 2021. https://doi.org/10.2514/6.2021-1745.

[24] Araya, G., Lagares, C., and Jansen, K., "Reynolds number dependency in supersonic spatially-developing turbulent boundary layers," *2020 AIAA SciTech Forum (AIAA 3247313) 6 - 10 January, Orlando, FL.*, 2020.

[25] Lagares, C. J., and Araya, G., "Power spectrum analysis in supersonic/hypersonic turbulent boundary layers," *AIAA SCITECH 2022 Forum*, 2022. https://doi.org/10.2514/6.2022-0479, URL https://arc.aiaa.org/doi/abs/10.2514/6.2022-0479.

[26] Lagares, C. J., and Araya, G., *Compressibility Effects on High-Reynolds Coherent Structures via Two-Point Correlations*, 2021. https://doi.org/10.2514/6.2021-2869, URL https://arc.aiaa.org/doi/abs/10.2514/6.2021-2869.

[27] Doosttalab, A., Araya, G., Newman, J., Adrian, R., Jansen, K., and Castillo, L., "Effect of small roughness elements on thermal statistics of a turbulent boundary layer at moderate Reynolds number," *Journal of Fluid Mechanics*, Vol. 787, 2015, pp. 84–115.

[28] Araya, G., Castillo, L., Meneveau, C., and Jansen, K., " A dynamic multi-scale approach for turbulent inflow boundary conditions in spatially evolving flows," *Journal of Fluid Mechanics*, Vol. 670, 2011, pp. 518–605.

[29] Lund, T., Wu, X., and Squires, K., "Generation of turbulent inflow data for spatially-developing boundary layer simulations," *Journal of Computational Physics*, Vol. 140, No. 2, 1998, pp. 233–258.

[30] Kistler, A., and Chen, W., "A Fluctuating Pressure Field in a Supersonic Turbulent Boundary Layer," *Journal of Fluid Mechanics*, Vol. 16, 1963, pp. 41–64.

[31] Urbin, G., and Knight, D., "Large-Eddy Simulation of a supersonic boundary layer using an unstructured grid," *AIAA Journal*, Vol. 39, No. 7, 2001, pp. 1288–1295.

[32] Favre, A., "Equations des gaz turbulents compressibles. I partie: Formes générales," *Journal de Mécanique*, Vol. 4, No. 3, 1965, pp. 361–390.

[33] Abadi, M., Agarwal, A., Barham, P., Brevdo, E., Chen, Z., Citro, C., Corrado, G. S., Davis, A., Dean, J., Devin, M., Ghemawat, S., Goodfellow, I., Harp, A., Irving, G., Isard, M., Jia, Y., Jozefowicz, R., Kaiser, L., Kudlur, M., Levenberg, J., Mané, D., Monga, R., Moore, S., Murray, D., Olah, C., Schuster, M., Shlens, J., Steiner, B., Sutskever, I., Talwar, K., Tucker, P., Vanhoucke, V., Vasudevan, V., Viégas, F., Vinyals, O., Warden, P., Wattenberg, M., Wicke, M., Yu, Y., and Zheng, X., "TensorFlow: Large-Scale Machine Learning on Heterogeneous Systems," , 2015. URL https://www.tensorflow.org/, software available from tensorflow.org.

[34] "MPI: A message passing interface," *Supercomputing '93:Proceedings of the 1993 ACM/IEEE Conference on Supercomputing*, 1993, pp. 878–883. https://doi.org/10.1109/SUPERC.1993.1263546.

[35] Schlatter, P., and Orlu, R., "Assessment of direct numerical simulation data of turbulent boundary layers," *Journal of Fluid Mechanics*, Vol. 659, 2010, pp. 116–126.

[36] Pirozzoli, S., and Bernardini, M., "Turbulence in supersonic boundary layers at moderate Reynolds number," *Journal of Fluid Mechanics*, Vol. 688, 2011, pp. 120–168. https://doi.org/10.1017/jfm.2011.368.

[37] Araya, G., Lagares, C., and Jansen, K., "Direct simulation of a Mach-5 turbulent spatially-developing boundary layer," *49^{th} AIAA Fluid Dynamics Conference, AIAA AVIATION Forum, (AIAA 3131876) 17 - 21 June, Dallas, TX*, 2019.

[38] Sutskever, I., Martens, J., Dahl, G., and Hinton, G. E., "On the importance of initialization and momentum in deep learning," *Proceedings of the 30th International Conference on Machine Learning*, Vol. 28, No. 3, 2013, pp. 1139–1147.

[39] Morkovin, M. V., "Effects of compressibility on turbulent flows," *Mecanique de la Turbulence*, Vol. 367, 1962.

[40] Schlichting, H., and Gersten, K., *Boundary-Layer Theory*, 9^{th} ed., Springer, 2000.

[41] Prandtl, L., *Essentials of Fluid Dynamics*, Blackie, 1952.

[42] White, F. M., *Fluid Mechanics*, 8^{th} ed., McGraw-Hill Education, 2015.